JOURNAL OF GEOPHYSICAL RESEARCH, VOL. 113, B07108, doi:10.1029/2007JB005213, 2008

Segmentation of the Blanco Transform Fault Zone from earthquake analysis: Complex tectonics of an oceanic transform fault

Jochen Braunmiller[1] and John Nábělek[1]

Received 7 June 2007; revised 31 December 2007; accepted 8 April 2008; published 24 July 2008.

[1] The Blanco Transform Fault Zone (BTFZ) forms the ~350 km long Pacific–Juan de Fuca plate boundary between the Gorda and Juan de Fuca ridges. Nearby broadband seismic networks provide a unique framework for a detailed, long-term seismotectonic study of an entire oceanic transform fault (OTF) system. We use regional waveforms to determine 129 earthquake source parameters; combined with 28 Harvard moment tensors, they represent the largest waveform derived OTF source parameter data set. Joint epicenter determination removes the northeasterly routine location bias. Projecting seismicity onto the BTFZ, we determine along-fault seismic slip rate variations. Earthquake source parameters and morphology indicate several transform segments separated by extensional step overs. The eastern segment from Gorda Ridge to Gorda Depression is a pull-apart basin. The longest transform (~150 km) following Blanco Ridge from the Gorda to Cascadia depression is seismically very active, seismically fully coupled, has a wider seismic zone (~9 km) than other BTFZ transform segments and accommodates the largest (M_w 6.4–6.5) BTFZ earthquakes. Interpretation of Cascadia Depression as spreading ridge is supported by plate motion parallel normal faulting T axes. Spreading is currently tectonic; 9 km deep earthquakes indicate a deep source for intermittent intrusives and rapid postemplacement cooling. A short transform connects to the pull-apart Surveyor Depression. Widely spread seismicity along the western BTFZ reflects complex morphology indicating ongoing plate boundary reorganization along short, narrow width subparallel faults. Seismic coupling is low in extensional (≤15%) compared to transform areas (35–100%), implying different mechanical properties. Centroid depth variations are consistent with seismic slip cutoff near 600°C.

Citation: Braunmiller, J., and J. Nábělek (2008), Segmentation of the Blanco Transform Fault Zone from earthquake analysis: Complex tectonics of an oceanic transform fault, *J. Geophys. Res.*, *113*, B07108, doi:10.1029/2007JB005213.

1. Introduction

[2] Oceanic transform fault systems (OTF) are a major plate boundary type connecting the mid-ocean ridge spreading centers along a total length of about 45,000 km [*Bird et al.*, 2002]. Their seismotectonic behavior is difficult to study, because most OTFs are located far from land seismic networks. Previous studies thus used teleseismic data, recorded several thousand kilometers away, to determine the source mechanisms and the distribution of the infrequent larger earthquakes to deduce the overall seismic character of OTFs [e.g., *Kanamori and Stewart*, 1976; *Burr and Solomon*, 1978; *Stewart and Okal*, 1983; *Engeln et al.*, 1986; *Goff et al.*, 1987; *Bergman and Solomon*, 1988; *Wolfe et al.*, 1993; *Abercrombie and Ekström*, 2003]. Major results include the observation of slow earthquakes [e.g., *Kanamori and Stewart*, 1976; *Okal and Stewart*, 1982; *Beroza and Jordan*, 1990], the depth dependence of seismic slip with lithospheric age [e.g., *Engeln et al.*, 1986; *Abercrombie and Ekström*, 2003] and the large variation of seismic coupling [e.g., *Brune*, 1968; *Bird et al.*, 2002; *Boettcher and Jordan*, 2004], i.e., the amount of plate motion explained by earthquakes, along these faults. From teleseismic distances, OTFs appear relatively simple compared to their continental counterparts and seismic properties are generally evaluated as averages over an entire OTF [e.g., *Langenhorst and Okal*, 2002; *Boettcher and Jordan*, 2004]. Detailed morphological studies [e.g., *Pockalny et al.*, 1988; *Embley and Wilson*, 1992; *Ligi et al.*, 2002], however, revealed considerable structural complexities that probably affect earthquake behavior along OTFs. Spatially variable, complex OTF seismicity patterns have not been investigated yet, because detailed studies, so far, were limited to short-term, spatially restricted ocean bottom seismometer (OBS) deployments [e.g., *Tréhu and Solomon*, 1983; *Wilcock et al.*, 1990]. The OBS studies analyzed the frequent microearthquakes, but it is not clear whether small events are relevant markers for long-term seismotectonic behavior. The establishment of a broadband seismic network along the coast of the northwestern United States and western Canada and data availability from

[1]College of Oceanic and Atmospheric Sciences, Oregon State University, Corvallis, Oregon, USA.

0148-0227/08/2007JB005213$09.00

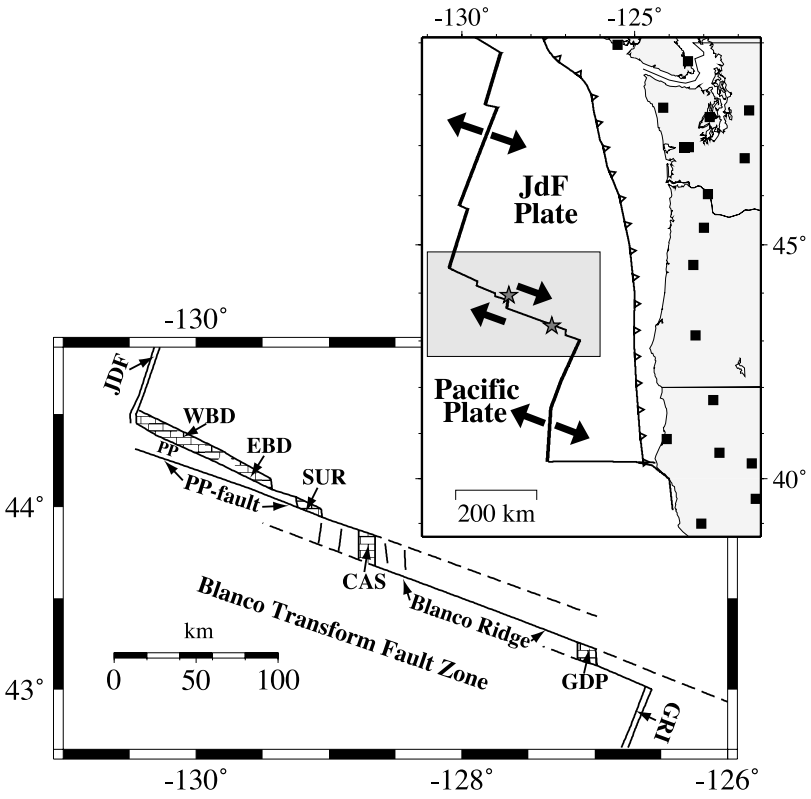

Figure 1. Schematic map of the Blanco Transform Fault Zone (BTFZ) following *Embley and Wilson* [1992]. Solid, northwest trending lines are active transforms; dashed lines are inactive fault traces. Basins are stippled; north trending solid lines near CAS are normal fault scarps. Juan de Fuca (JDF) and Gorda (GRI) ridges are shown as double lines. GDP, CAS, SUR, EBD, and WBD are the Gorda, Cascadia, Surveyor, East Blanco, and West Blanco depressions; PP refers to Parks Plateau. The top right inset is a tectonic overview of the study area (gray box). Squares show coastal broadband seismic stations (stations inland not shown). Solid arrows are plate motion vectors of the Juan de Fuca (JDF) plate relative to the Pacific (~6 cm/a) plate based on the work by *Wilson* [1993]. Solid lines along the BTFZ are active plate boundaries in the *Embley and Wilson* [1992] model. Stars mark locations of earthquakes used to illustrate waveform fits (Figures 3 and 4).

Navy's offshore Sound Surveillance System (SOSUS) hydrophone arrays for earthquake studies provide a unique framework for a detailed long-term seismotectonic study of an entire OTF, the Blanco Transform Fault Zone (BTFZ).

[3] The BTFZ is ~350 km long and forms the Pacific–Juan de Fuca plate boundary between the Gorda and the Juan de Fuca ridges in the northeast Pacific Ocean (Figure 1). *Embley and Wilson* [1992] used high-resolution SeaBeam bathymetry to divide the BTFZ into five transform fault segments separated by deep basins. The easternmost segment connects the Gorda Ridge with the Gorda Depression. The 150 km long continuous segment along the Blanco Ridge from the Gorda Depression to the Cascadia Depression is the dominant feature in the eastern BTFZ [*Ibach*, 1981; *Embley and Wilson*, 1992; *Dziak et al.*, 2000]. Three short transform segments along BTFZ's western part connect the Cascadia, Surveyor, and East Blanco depressions with the Juan de Fuca ridge. The Parks Plateau lineation, which runs for about 150 km in a northwestward direction from the Cascadia Depression, forms the southern boundary of the Parks Plateau. The lineation has been interpreted as a formerly [*Embley and Wilson*, 1992; *Dauteuil*, 1995] or currently [*Delaney et al.*, 1981] active transform fault. The central Cascadia Depression is the largest basin. Basement doming inferred from seismic reflection data indicates active seafloor spreading [*DeCharon*, 1989; *Embley and Wilson*, 1992]. The smaller Gorda, Surveyor, and East Blanco depressions appear to be oceanic analogs to pull-apart structures found along divergent continental wrench-fault systems [*Embley and Wilson*, 1992].

[4] The BTFZ is seismically very active [e.g., *Tobin and Sykes*, 1968; *Bolt et al.*, 1968; *Chandra*, 1974; *Dziak et al.*, 1991], but the lack of precise earthquake locations and source mechanisms has prevented a detailed seismotectonic analysis before. We used data from the broadband seismic network to determine the source mechanisms of the frequent, small magnitude $M \geq 4$ earthquakes that are distributed over the entire BTFZ for the period 1994–1998 by modeling regional waveforms [*Nábělek and Xia*, 1995]. We added Harvard centroid moment tensor solutions [*Dziewonski et al.*, 1994, and references therein] to include significant events to our tectonic study that occurred since 1976, predating regional analysis and to verify regional results by comparing events analyzed by both methods. Both methods use robust waveform matching techniques providing reliable earthquake source parameters that reveal deformation style varia-

Table 1. Crustal Layer Parameters Used for Calculation of Synthetic Seismograms

Thickness (km)	v_p (km/s)	v_s (km/s)	Density (g/cm^3)
1.50	4.20	2.07	2.55
1.80	6.00	3.02	2.75
3.70	6.90	3.48	3.00
half-space	8.10	4.33	3.35

tions along the BTFZ and supply accurate size estimates. We also relocated larger earthquakes using the joint epicenter determination technique [*Douglas*, 1967; *Dewey*, 1972] because routine land-based locations are systematically shifted to the northeast of the BTFZ [e.g., *Dziak et al.*, 1991; *Cronin and Sverdrup*, 2003].

[5] Our resulting data present the most comprehensive and detailed image of seismic activity and deformation along any OTF system to date. With our data, we revisit BTFZ segmentation and Pacific–Juan de Fuca plate boundary configuration, infer the depth extent of faulting, examine the seismic slip rate and slip distribution, and compare relocations with SOSUS locations.

2. Methods and Results

2.1. Earthquake Moment Tensors

[6] The broadband seismic network (Figure 1) consists of more than 20 digital three-component broadband, high-dynamic range stations distributed along coastal northern California, Oregon, Washington, and British Columbia. The network provides data of unprecedented quality that allows reliable determination of source parameters of magnitude $M \geq 4.0$ earthquakes since 1994, when station density became sufficient for analysis.

[7] We inverted complete three-component regional seismograms for the earthquake source parameters (deviatoric seismic moment tensor) by minimizing the least squares misfit between observed and synthetic seismograms. Strike, dip, rake, and seismic moment follow from the moment tensor [e.g., *Aki and Richards*, 1980]. Centroid depth was found by grid search over trial depths of 4, 6, 9, 12 and 15 km. We inverted all data simultaneously at low frequencies where regional seismograms are dominated by guided waves and surface waves, which can be modeled adequately by a simple 1-D velocity depth structure (Table 1). Synthetic seismograms were calculated with a discrete wave number algorithm [*Bouchon*, 1982]. The frequency band used depends on earthquake size and signal-to-noise ratio. In most cases, we used the 0.02–0.05 or 0.02–0.04 Hz bands; for larger events with stronger long-period signal, we lowered the high-pass to 0.01 Hz. We used three-component data whenever possible and discarded only noisy traces resulting, on average, in 25–30 waveforms from more than a dozen stations for each event. For details, see *Nábělek and Xia* [1995] and *Braunmiller and Nábělek* [2002].

[8] Routine analysis began in January 1994 and until November 1998 we determined 129 regional moment tensor (RMT) solutions for earthquakes occurring between 42.6°–45°N and 126°–131°W (Table 2). The data set includes four pre-1994 events large enough for analysis with data from the few broadband stations operating in the early 1990s. Three normal faulting events south of 43°N occurred on the Gorda Ridge; the remaining 126 events are distributed along the entire BTFZ. Strike-slip mechanisms dominate with normal faulting events generally confined to the basins. From investigations of parameter uncertainties based on variance increase relative to a best fit model [*Braunmiller et al.*, 1995, *Braunmiller and Nábělek*, 2002] and considering the good station coverage that includes nodal and antinodal arrivals on three-component data, we estimate average uncertainties in strike, dip, and rake for individual events of ±5°, ±15°, and ±20°, respectively. As an entity, our results are highly consistent (see section 3.2) suggesting that statistical errors are actually smaller. Systematic errors are difficult to deduce; for strike, considering the agreement with morphological trends, such effects are unlikely suggesting that our average slip vector directions are probably good to within a few degrees.

[9] Earthquake size ranges from moment magnitude M_w = 3.8 to 6.5 (Figure 2, top). For the 5-year analysis period, the distribution appears complete for $4.6 \leq M_w \leq 5.4$. The slope b of the frequency-size distribution (Figure 2, middle) describing the relative occurrence rate of small to large events is 1 in this magnitude range consistent with global averages [e.g., *Scholz*, 2002].

[10] The centroid depths are generally shallow (Figure 2, bottom). Depth is obtained through a grid search providing no formal uncertainty estimates. We assigned quality levels (Table 2) based on a 5% variance increase relative to the best fit depth. Long-period inversions are unstable for very shallow grid points forcing us to invert only for depths of 4 km and more, a shallow (upper) 5% bound is thus seldom defined. We assign quality A, B, and C when the lower 5% bound is within 3, 5, and 8 km from the best depth, respectively, resulting in 49 A, 60 B, and 15 C quality events. Quality C is usually restricted to smaller $M_w < 4.5$ events indicating that higher noise levels affect variance reduction. No C event has a best depth deeper than 6 km. Overall, depth is slightly better constrained for normal faulting than for strike slip events reflecting a larger contribution of depth sensitive Rayleigh wave energy. Depth was fixed for four events (quality F). One earthquake, immediately preceding a stronger event, has no defined lower bound (quality D). Small changes to the oceanic velocity model used to calculate theoretical seismograms had no significant effect on estimated event depth.

[11] Figures 3 and 4 show result examples for representative midsized events; for larger events, waveform fits and parameter resolution are usually even better. Figure 3 (top) shows waveform fits for the 4 January 1998 M_w = 4.8 normal faulting event inside the Cascadia Depression. Azimuthal amplitude variations and use of three component data constrain source type and fault plane orientations tightly. Note the systematic amplitude increase on vertical components from north (station PHC) to east (YBH) and the subsequent decrease toward southeast (BKS) and the overall larger amplitudes on vertical than on transverse components. Figure 3 (bottom) shows centroid depth is well resolved (quality A), and source mechanism and M_w estimates are robust.

[12] Figure 4 shows fits for the 19 October 1997 M_w = 4.5 Blanco Ridge strike-slip event. The mechanism, particularly the nodal planes' strikes, are well constrained by vertical component recordings that show a four-lobed radi-

Table 2. Regional Moment Tensor Solutions[a]

Date	Lat (°N)	Lon (°W)	LS	S/D/R (deg)	M_w	CD (km)	DC (%)	CO
9002121344	43.934	−128.976	R	165/52/−107	5.63	6 A	82	6
9208210102	43.797	−128.457	R	198/26/−61	5.54	6 A	98	12
9211172037	43.733	−128.647	R	226/42/−43	5.20	6 B	60	13
9305092216	43.524	−128.254	R	301/84/−131	5.20	6 B	83	18
9401190116	43.437	−127.806	R	299/68/−153	5.74	9 B	65	29
9402282151	44.319	−130.112	N	124/78/−176	5.42	6 D	94	32
9402282153	44.434	−130.025	R	294/79/−17	5.70	4 B	98	33
9405111254	44.324	−130.101	N	288/62/−144	4.72	6 B	62	16
9406140204	43.580	−128.237	N	296/70/−140	4.82	6 B	55	18
9406300730	43.537	−128.314	N	294/83/−133	4.77	6 B	56	24
9407131752	43.266	−127.044	R	307/85/−124	4.99	6 B	84	19
9407222244	43.121	−127.040	N	304/69/−144	4.16	6 A	99	7
9408121126	43.832	−128.695	N	282/58/178	4.01	9 A	26	9
9410251559	44.150	−129.655	N	300/73/−147	5.05	9 A	71	21
9410270438	43.025	−126.248	N	303/81/−146	4.53	6 A	52	12
9410271745	43.427	−127.549	R	295/75/−158	6.48	9 A	73	63
BW				290/87/175	6.44	6.5		
9410282002	43.798	−128.489	J	1/65/−97	4.44	6 B	93	21
9410300223	43.306	−127.234	N	299/73/−144	4.70	9 B	100	20
9410302054	43.486	−128.072	N	304/76/−142	4.37	6 C	51	10
9411022048	43.550	−128.018	N	298/87/−124	4.97	4 A	85	19
9411060404	43.288	−127.174	N	301/76/−143	4.78	6 B	84	20
9411071502	43.294	−127.143	N	300/88/−133	4.38	6 B	96	12
9411222123	43.406	−127.553	N	297/75/−162	5.00	6 B	71	19
9412210742	44.400	−129.900	J	299/81/−133	4.52	6 B	70	13
9502221019	43.079	−126.651	J	302/76/−150	4.28	6 B	70	20
9503280343	43.233	−127.077	N	304/61/−150	4.04	6 A	86	15
9504221423	44.147	−129.657	N	294/73/−145	4.62	6 B	80	24
9505040618	43.022	−126.701	N	339/62/−91	4.16	6 B	65	12
9505122350	43.392	−127.442	N	301/71/−159	4.14	6 A	91	10
9505130603	43.389	−127.442	N	117/88/141	4.73	6 A	20	21
9506092136	43.941	−129.224	J	290/83/−163	4.56	6 B	75	24
9507090616	44.466	−130.377	N	129/79/148	4.69	6 F	16	30
9507090618	44.526	−130.308	N	126/70/170	4.55	6 F	82	29
9508030541	43.160	−126.782	N	117/58/−176	4.24	6 B	17	25
9508142132	44.049	−128.720	R	5/63/−81	4.69	6 A	90	22
9508151057	43.852	−128.888	N	331/65/−105	4.21	6 C	98	19
9508260541	43.437	−127.558	J	112/88/151	4.10	4 B	25	26
9509020941	43.812	−128.693	N	12/62/−96	4.61	9 A	61	26
9509231826	44.309	−130.041	N	291/49/−161	4.10	4 C	52	14
9509250758	43.828	−128.906	N	19/64/−90	5.00	9 B	66	36
9509250801	43.899	−128.834	N	14/62/−88	4.50	9 B	52	23
9509251909	43.760	−128.532	R	11/63/−91	4.83	9 A	56	26
9509260139	43.209	−127.277	R	295/84/−155	5.35	6 B	69	42
9510070827	43.924	−129.260	R	350/60/−97	4.96	6 A	74	33
9510070857	44.034	−129.191	N	350/63/−94	4.35	6 A	62	21
9510071058	43.982	−129.043	N	353/66/−89	5.09	6 A	100	23
9510081803	44.014	−129.127	N	346/62/−91	4.42	6 B	61	16
9510150649	43.633	−128.552	N	299/70/−165	3.79	6 F	73	8
9510191500	43.292	−127.257	N	291/80/−173	4.28	4 A	50	21
9511160114	44.302	−129.815	J	289/76/−156	4.65	6 A	91	33
9511230040	44.153	−129.616	J	120/66/−171	4.51	6 C	15	30
9512051503	43.423	−127.634	J	108/75/170	4.31	4 C	41	29
9512130715	43.422	−127.606	J	295/73/−174	4.58	6 B	49	18
9512240251	43.132	−126.941	N	297/83/−136	4.55	4 B	99	27
9601090737	43.139	−126.497	R	296/85/−160	5.22	4 A	61	35
9601170216	43.877	−128.452	J	9/58/−98	4.79	9 B	56	29
9601170758	43.836	−128.769	J	291/56/−162	4.75	6 A	50	30
9601170825	43.890	−128.762	J	293/55/−162	5.12	6 A	24	31
9602060532	43.598	−128.388	N	301/72/−162	4.14	4 B	67	20
9602060540	42.688	−126.761	N	26/56/−74	4.55	6 B	64	26
9602082132	44.041	−129.315	N	283/88/−172	4.14	6 F	56	16
9602200052	43.355	−126.731	R	296/72/−153	5.26	4 C	99	43
9602200121	43.275	−127.107	N	111/89/173	4.44	6 B	54	25
9603152241	42.914	−126.675	N	26/50/−81	3.93	6 A	85	26
9603281141	43.213	−127.040	J	283/77/−167	4.34	4 C	30	7
9604090748	43.948	−129.148	N	295/68/−161	4.57	6 B	99	37
9604151229	43.456	−127.652	R	110/85/149	5.41	4 A	63	55
9604291139	44.326	−129.882	J	296/58/−156	4.31	6 B	91	32
9605030029	44.373	−130.154	N	115/72/−145	4.10	4 A	99	18
9605181914	43.336	−127.434	N	109/82/171	4.50	4 B	58	29
9605220302	43.923	−129.242	J	106/88/168	4.26	6 B	61	29
9607172236	43.161	−127.055	N	341/50/−89	4.23	6 B	76	24

Table 2. (continued)

Date	Lat (°N)	Lon (°W)	LS	S/D/R (deg)	M_w	CD (km)	DC (%)	CO
9607281500	43.038	−126.842	J	116/86/160	4.25	6 C	35	26
9608260711	43.816	−128.434	J	16/64/−89	4.91	9 B	75	38
9610012209	43.924	−129.062	N	352/49/−86	4.53	6 B	100	37
9610030725	43.964	−129.022	N	346/56/−91	4.50	12 A	59	31
9610031000	43.941	−128.972	N	343/62/−93	4.99	9 A	94	37
9610031009	43.931	−129.128	R	342/60/−95	5.32	9 B	99	47
9610161250	43.344	−127.596	N	302/61/−157	4.37	6 B	71	28
9610161307	43.337	−127.580	N	300/68/−151	4.15	9 B	82	25
9611040012	43.974	−129.162	N	290/73/−148	4.45	4 A	61	32
9611042254	43.503	−127.355	R	298/73/−157	5.47	6 A	83	41
9611080551	44.347	−130.205	N	295/78/−153	4.64	4 A	58	31
9611080555	44.329	−130.210	N	295/75/−140	4.71	4 A	72	31
9611192220	43.139	−126.912	N	193/33/−60	4.47	6 A	42	20
9611241822	43.179	−126.969	N	181/42/−54	4.43	6 B	23	20
9612080348	43.843	−129.573	R	289/89/−163	5.27	4 A	77	61
9612080542	43.938	−129.402	R	285/89/−150	4.93	4 A	76	39
9701131632	43.561	−128.233	N	291/76/−147	4.49	4 B	71	32
9702201103	43.287	−127.398	N	294/81/−153	4.51	6 B	93	24
9703231641	43.354	−127.361	R	298/82/−141	4.71	4 B	70	31
9704121641	43.129	−126.717	N	119/86/166	4.81	6 B	38	29
9704170944	44.412	−130.445	N	335/57/−91	4.25	12 A	68	23
9704171417	44.329	−129.922	N	290/81/−142	4.79	4 B	78	45
9705271531	43.198	−127.307	N	116/59/−176	4.28	6 C	72	28
9705282303	43.356	−127.511	N	295/88/−162	4.51	4 A	68	37
9706092120	43.863	−128.671	N	306/54/−127	4.11	6 B	69	24
9707071325	43.425	−127.532	R	109/76/−175	5.18	4 B	74	57
9707101848	44.180	−129.417	R	118/77/176	4.79	6 A	39	26
9707110203	44.205	−129.273	R	116/83/177	5.42	4 B	63	53
9707111752	44.083	−129.495	N	296/72/−123	4.57	4 A	82	24
9710010628	43.138	−127.205	N	318/76/162	4.31	6 C	80	33
9710050142	43.206	−127.114	N	299/74/−158	4.06	6 C	64	12
9710111543	44.272	−130.075	N	289/79/175	4.70	4 A	73	46
9710111554	44.228	−129.928	R	110/88/−180	5.47	4 A	62	50
9710190409	43.324	−127.404	J	292/73/−166	4.48	9 B	75	32
9710220234	44.277	−129.872	J	294/54/−167	4.09	4 A	79	20
9712030943	43.287	−127.784	N	290/84/−174	4.38	4 A	80	26
9801041833	43.958	−128.641	N	6/65/−93	4.79	9 A	96	33
9801061114	44.306	−129.987	N	291/55/−169	4.07	6 C	81	21
9801080329	42.851	−126.582	N	35/66/−66	4.51	9 A	65	15
9801190038	44.019	−129.285	N	289/75/−165	4.17	4 B	85	13
9801262325	44.043	−129.273	N	295/89/−144	4.82	4 B	64	41
9803230228	43.357	−127.057	R	113/89/173	5.25	6 A	64	56
9803261224	43.317	−127.589	N	295/67/−159	4.53	9 A	57	35
9804030842	43.093	−126.770	N	117/75/174	4.41	6 B	38	23
9804200648	44.045	−129.350	N	286/78/−154	4.14	6 C	81	27
9804211838	44.181	−129.698	N	291/72/−157	4.41	4 B	51	29
9806050604	43.221	−127.579	N	291/68/−158	4.15	6 A	65	28
9806060708	42.960	−126.794	N	296/79/−175	4.27	6 A	30	23
9806251112	43.228	−127.355	N	118/78/−154	4.03	6 B	13	26
9807141613	43.984	−129.307	N	290/59/−158	4.19	4 B	64	24
9808020751	42.947	−126.517	N	119/79/−149	4.00	6 B	68	20
9808250034	43.189	−127.230	N	299/68/−153	4.15	4 C	79	17
9809061234	43.317	−127.584	N	298/67/−155	4.70	9 B	83	34
9809241322	42.975	−126.642	N	295/80/179	4.77	4 B	42	47
9809251444	43.187	−127.185	N	295/68/−163	4.14	4 B	88	25
9811012123	43.008	−126.707	N	293/87/−174	4.36	4 C	53	32
9811081510	43.991	−129.129	N	289/73/−148	4.44	4 A	53	30

[a]Date: year month day hour minute; Lat, Lon, latitude and longitude; LS, location source; R, relocated; N, NOAA-PMEL; J, at OSU using regional P and S arrivals; S/D/R, strike, dip, and rake; M_w, moment magnitude following *Hanks and Kanamori* [1979]; CD, centroid depth and assigned quality; depth relative to ocean floor; DC, double couple percentage, where DC = $(1-2\,\varepsilon) \times 100$[%], ε = |smallest|/|largest| moment tensor eigenvalue; CO, number of components (vertical, radial, transverse) used; BW, teleseismic body wave inversion result for the 9410271745 event.

ation pattern typical for strike-slip earthquakes. Note the waveform differences compared to the normal faulting event in Figure 3. The transverse component is nodal at COR and the northwest–southeast trending nodal plane causes nodal vertical and radial waveforms and large antinodal transverse waveforms at YBH. Even though this is a smaller event, centroid depth (quality B), source mechanism and M_w estimates are robust (Figure 3, bottom).

[13] In addition to our RMT solutions, we used source parameter estimates from the 28 Harvard centroid moment tensor (CMT) solutions available for the BTFZ from 1976 until 1998 (Table 3). Seventeen CMT events, predating regional data analysis, were added to our source parameter

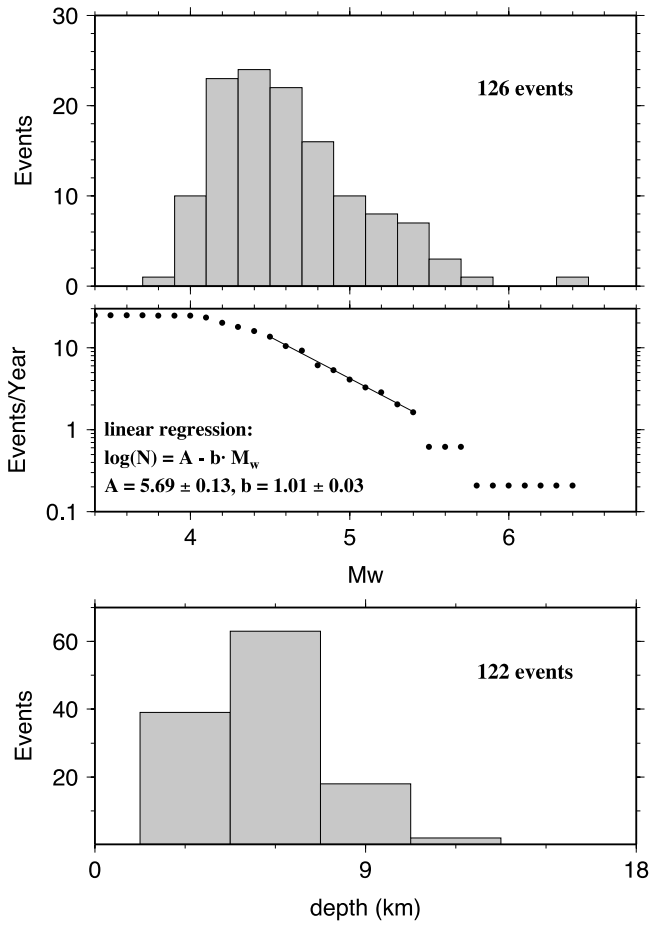

Figure 2. Size and depth distribution of RMT solutions along the BTFZ. (top) Histogram of event moment magnitudes M_w. (middle) Number of events per year (N) greater or equal M_w versus M_w. Linear regression was performed in magnitude range covered by solid line. (bottom) Histogram of event centroid depths; only events with resolved depth are shown.

database to derive seismotectonic interpretations. For eleven earthquakes common to both data sets, CMT solutions were used to verify reliability of RMT results. The solutions generally agree except for the 12 February 1990 event where the CMT solution was constrained to be either pure strike slip or 45° dip slip ($m_{xz} = m_{yz} = 0$). The median P wave radiation pattern similarity of $\eta_p = 0.92$ is above the 0.88 value found by *Helffrich* [1997] when comparing the Harvard, U.S. Geological Survey, and Earthquake Research Institute at the University of Tokyo catalogs, the median mean principal axes difference $|\Delta Ax|$ [*Bernardi et al.*, 2004] is only 14°, and the median difference of the horizontal slip vector directions of the seven strike-slip events is a mere 3°. The M_w estimates are also highly consistent with a median difference between RMT and CMT solutions of 0.05 units. Depth of most CMT solutions was constrained to 15 km because long-period teleseismic analysis becomes unstable for shallow depths; RMT solutions thus provide important constraints on depth for these events.

[14] Comparing the M_w estimates with body (m_b) and surface wave (M_S) magnitudes from the International Seismological Centre (ISC) and the U.S. Geological Survey's Preliminary Determination of Epicenter (PDE) databases reveals significant differences (Figure 5). The large average 0.5 magnitude unit M_w-m_b difference (long dashes) underestimates seismic moment M_0 more than fivefold if m_b would be converted straight to M_0 assuming m_b equals M_w. Linear regression is not a better description of the M_w-m_b relation because data scatter is large; we used the average difference for later m_b-to-M_0 conversion (see below). M_S also underestimates M_w. Linear regression yields $M_w = 2.40 + 0.62\ M_S$ consistent with global relations [*Ekström and Dziewonski*, 1988]. We excluded $M_S < 4$ events from regression, because for small events M_S is generally based on few, possibly dubious amplitude readings. For M = 6.3 events, M_w and M_S appear equivalent. An M_S-m_b discrepancy, comparable to our 0.5 M_w-m_b difference, has been noted for OTF earthquakes [*Stewart and Okal*, 1981].

2.2. Earthquake Relocations

[15] Routine earthquake locations along the BTFZ are scattered and systematically shifted to the northeast of the bathymetric features that define the plate boundary (Figure 6). We used the joint epicenter determination (JED) technique [*Douglas*, 1967; *Dewey*, 1972] to relocate larger, tectonically significant events. Our data are teleseismic P wave arrival time picks from the ISC for the

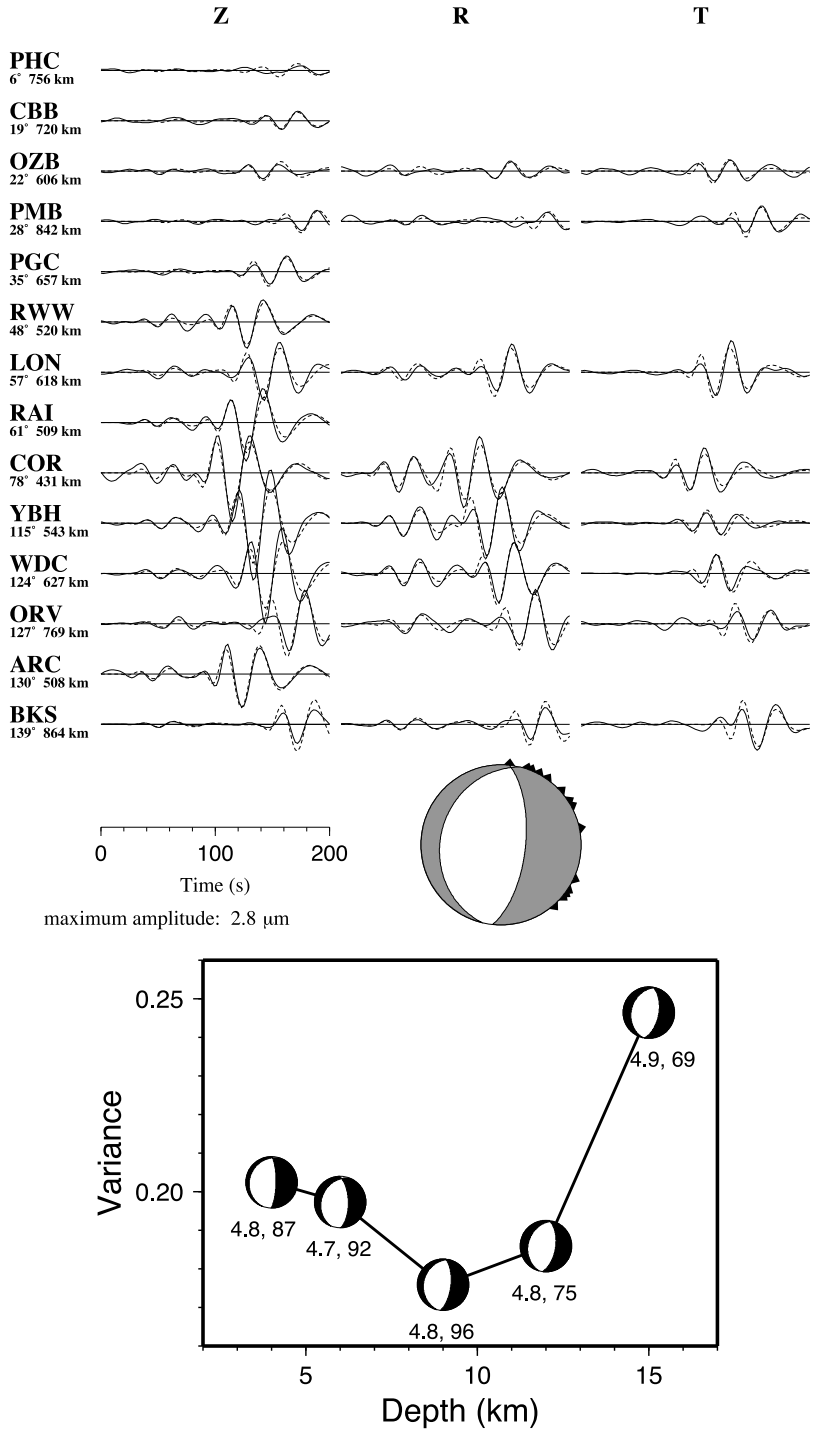

Figure 3. (top) Observed (solid) and synthetic (dashed) seismograms for best fit model in the 25 to 50 s period passband for the 4 January 1998 $M_w = 4.8$ normal faulting earthquake in the Cascadia Depression. Z, R, and T are vertical, radial, and transverse components. Stations are in azimuthal order with numbers beneath station codes giving event-station azimuth and distance. Triangles on fault plane solution (lower hemisphere projection) depict azimuthal coverage. All seismograms are normalized to 100 km epicentral distance assuming cylindrical geometrical spreading. (bottom) Residual variance reduction versus centroid depth. Numbers are moment magnitude and percent double couple of moment tensor solution. Centroid depth is quality A.

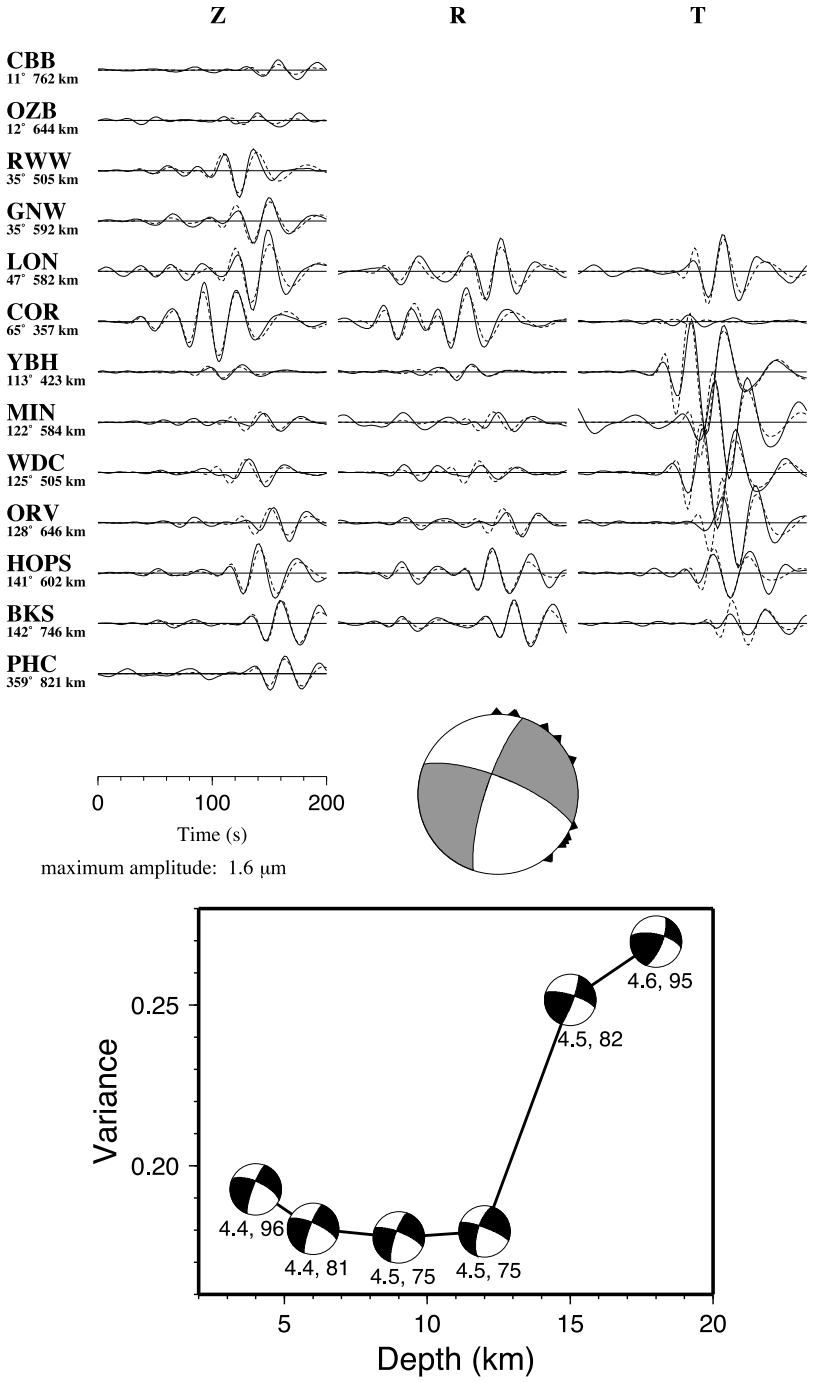

Figure 4. Waveform fit and variance versus centroid depth for the 19 October 1997 $M_w = 4.5$ strike-slip earthquake on the Blanco Ridge. Centroid depth is quality B. Otherwise, same as Figure 3.

period 1964–1995 and from the U.S. Geological Survey for the period 1996 to August 1998. Requiring a minimum of 20 teleseismic (event-station distance $18° \leq \Delta \leq 100°$) P picks resulted in a 144-event data set. Because of poor depth resolution of teleseismic data, all hypocenter depths were fixed at 10 km.

[16] To stabilize the inversion, we relocated all earthquakes relative to the $M_w = 6.5$ 13 March 1985 event (Table 3) because it has the most P picks (355). The ISC locations of this and of three other large events near Blanco Ridge (between 127.5° and 128°W, Figure 6) are closer to the plate boundary than most other events. It appears their absolute location are more accurate than for smaller events, probably due to a more even azimuthal station distribution and a larger number of P picks. We also performed JED inversions holding other events or event groups fixed and found relative locations of the 144 events with respect to each other are well constrained changing by less than ±3–5 km independently of the reference event.

[17] The greatly improved relative location resolution is the main advantage of JED over single event locations. We then shifted the entire cluster such that the reference

Table 3. Harvard Centroid Moment Tensor Solutions[a]

Date	Lat (°N)	Lon (°W)	S/D/R (deg)	M_w	CD (km)	DC (%)
7707281522	43.977	−129.225	306/75/−167	5.78	15[b]	75
8003301349	43.308	−127.251	120/86/156	5.57	15[b]	86
8111031347	43.358	−127.828	297/90/180[c]	6.44	10.1	87
8111221137	43.547	−127.232	115/87/−178	5.86	15[b]	94
8211131544	44.124	−129.643	287/90/180[c]	5.68	15[b]	84
8503131934	43.404	−127.669	297/72/−172	6.46	10.0	86
8601300715	43.352	−127.548	295/90/180[c]	5.26	15[b]	92
8610052157	43.330	−127.353	295/81/−170	5.63	15[b]	91
8706270601	43.321	−127.300	294/76/−173	5.40	15[b]	87
8710170812	43.240	−126.738	298/12/180	5.42	15[b]	96
8712071748	43.293	−127.345	115/84/−168	5.18	15[b]	98
8810231348	43.996	−129.863	294/90/180[c]	5.51	15[b]	67
8901111223	44.394	−129.765	332/43/−81	5.07	15[b]	19
8905161221	43.403	−127.753	295/76/−168	5.58	15[b]	75
9001161257	43.599	−127.112	117/82/−177	5.59	15[b]	98
9001171205	43.452	−127.545	118/83/165	5.68	15[b]	96
9002121344	43.934	−128.976	150/90/−180[c]	5.47	15[b]	56
9208041427	43.510	−127.141	116/80/−178	5.66	15[b]	82
9208210102	43.797	−128.457	214/28/−55	5.42	15[b]	15
9402282152	44.434	−130.025	299/78/−169	5.62	15[b]	97
9410271745	43.427	−127.549	296/88/−175	6.33	15[b]	97
9604151229	43.456	−127.652	113/74/179	5.37	15[b]	74
9610031009	43.931	−129.128	181/20/−78	5.36	15[b]	85
9611042254	43.503	−127.355	295/76/−169	5.45	15[b]	74
9612080348	43.843	−129.573	295/90/−180[c]	5.16	15[b]	64
9707110203	44.205	−129.273	301/81/−172	5.40	15[b]	89
9710111554	44.228	−129.928	298/82/−167	5.42	15[b]	90
9803230228	43.357	−127.057	293/84/162	5.24	15[b]	84

[a]Date, year month day hour minute; Lat, Lon, relocated latitude and longitude. Source information is taken from *Dziewonski et al.* [1994] and related sources. S/D/R, strike, dip, and rake.
[b]CD, centroid depth constrained. DC, double−couple percentage.
[c]Constrained $M_{xz} = M_{yz} = 0$. M_w, moment magnitude following *Hanks and Kanamori* [1979].

strike-slip event is on Blanco Ridge; its most likely location considering the active transform fault probably runs along the Blanco Ridge [*Dziak et al.*, 2000]. This shift was about 12 km in a southerly 200° azimuth direction, which is the smallest possible shift to bring the reference event from its ISC location onto Blanco Ridge at 43.404°N, 127.669°W. Relocations in Figures 8, 10, 11, 12, 13, 14, 16, and 17 are relative to this shifted epicenter.

[18] Figure 7 (top) shows relocation results; open circles are relocated epicenters with thin lines pointing to their original locations. The average shift is ∼30–40 km to the south-southwest consistent with results by *Cronin and Sverdrup* [2003], who relocated 120 $m_b > 5.0$ BTFZ earthquakes. Only a part is due to the overall 12 km shift of the cluster; the remainder is due to relative relocation shifts. Although shifting the 13 March 1985 event onto Blanco Ridge is not unique, the chosen shift results in relocations that are consistent with BTFZ's bathymetry. The eastern and western event boundaries now coincide closely with the Gorda and the Juan de Fuca ridges, respectively, and relocated events near the Cascadia Depression have normal faulting mechanisms. However, shifting the cluster an additional ±10–15 km along or ±5–10 km perpendicular to the BTFZ is possible without significantly degrading the match between epicenter distribution and bathymetry.

[19] The relocated epicenter distribution differs markedly between the eastern and western BTFZ (Figure 7). East of the Cascadia Depression (near 128.6°W), most events occurred close to and follow the Blanco Ridge between ∼127°–127.8°W. Activity is also concentrated in the Cascadia Depression. Further west, the distribution remains scattered. Additional tests relocating only events along BTFZ's western part showed the spread is not an artifact caused by the larger number of arrival times for events near Blanco Ridge. The spread is consistent with the complex morphology of the western BTFZ [*Embley and Wilson*, 1992] and suggests that the plate motion is distributed along several active fault strands.

[20] Unless noted, we consider in the following only the 123 well-relocated epicenters (Figure 7, bottom) with latitude and longitude uncertainties of less than 12 km at the 95% confidence limit. Larger uncertainties for other events indicate inconsistent arrival times resulting in large shifts or shifts in a direction significantly different from the average. Removing these events decreases the scatter in the relocated epicenters. Generally, larger ($M \geq 5$) events have more P picks and thus well-constrained epicenters.

3. Discussion

3.1. Comparison Between JED and SOSUS Locations

[21] The SOSUS hydrophone arrays, operated by the U.S. Navy, are designed to record long-range hydroacoustic signals for military purposes. Several arrays are located in the northeast Pacific, though their exact placement is secret. Researchers at the U. S. National Oceanic and Atmospheric Agency laboratory in Newport, Oregon were granted access to these arrays in 1993 and began locating earthquakes in the Juan de Fuca region. The very slow, well-known propagation speed of acoustic signals in the water column (T phases) permits a precise location of the signals' sources. SOSUS locations of five explosions on the Juan de Fuca

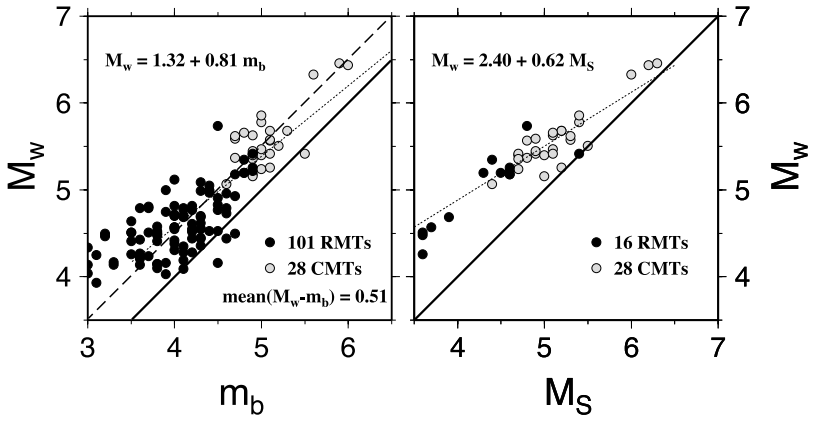

Figure 5. (left) Moment magnitude (M_w) versus body wave magnitude (m_b). (right) M_w versus surface wave magnitude (M_S). Black circles indicate RMT; gray circles indicate CMT solutions. For a one-to-one correspondence between magnitudes, all circles would fall on the diagonal (solid line). M_w versus m_b, on average, M_w is 0.51 units bigger than m_b (long dashes); a least squares fit (short dashes), $M_w = 1.32 + 0.81\ m_b$ (for $m_b \geq 3.5$) fits not significantly better than the average difference. M_w versus M_S, linear regression yields $M_w = 2.40 + 0.62\ M_S$ (for $M_S \geq 4.0$).

ridge were on average within 2 km of their actual location [*Fox et al.*, 1995]. This accuracy is comparable to quality earthquake locations within a local land network. Efficient propagation of acoustic signals in water also lowers the detection threshold for offshore earthquakes by more than a magnitude unit compared to land seismic networks [*Fox et al.*, 1994]. Detection of otherwise unnoticed earthquake swarms along the Juan de Fuca Ridge and the western BTFZ underscores the usefulness of SOSUS array data for studies of oceanic ridge-transform systems [*Dziak et al.*, 2006]. Rapid response efforts [*Embley et al.*, 1995; *Dziak et al.*, 1996; *Johnson et al.*, 2000] found anomalies in the water column and on the ocean floor near the swarm locations suggesting that SOSUS earthquake locations are accurate.

[22] The relationship between earthquake epicenters and the T phase generation mechanism [*Tolstoy and Ewing*, 1950; *Biot*, 1952; *Johnson et al.*, 1967], however, is not fully understood. Our high-precision JED relative locations provide an independent check for the accuracy and consistency of SOSUS locations. Of 144 relocated events, 24 were also located with SOSUS data (R. Dziak, personal communication, 1998). If both data sets were internally consistent (i.e., their relative locations identical), a simple translation would result in coinciding locations. This is not the case (Figure 8). Direction and distance from JED (open circles) to SOSUS locations (solid squares) vary considerably. In most cases, the SOSUS location falls outside the relocation's 95% confidence ellipsoid (including the overall 12 km shift) even when considering more conservative SOSUS location uncertainties of about ±10 km as suggested by *Johnson et al.* [2000] for earthquakes along the Juan de Fuca Ridge. Near the Blanco Ridge, location differences are primarily along ridge. In the western BTFZ, SOSUS locations are generally closer to bathymetric, probably tectonically active features (solid lines in Figure 8) than the more widely scattered relocated epicenters. Proximity of SOSUS locations to bathymetric features could indicate location precision. However, T phase energy transmission into the water column is more efficient in areas of rough or steep bathymetry [*Soukup and Odom*, 2001]. This effect could bias SOSUS locations toward such bathymetric features, because the locations, due to the emergent nature of T phases, are determined from arrival times of the peak amplitudes of the T phase envelopes.

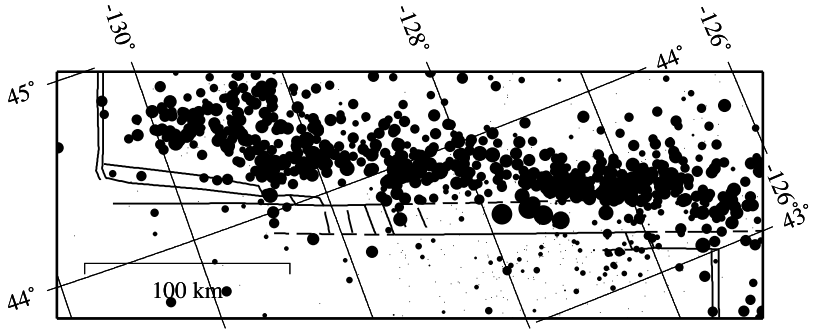

Figure 6. Earthquake epicenter distribution from ISC (1964–1995) and PDE (1996–08/1998). Note systematic epicenter shift to the northeast of the BTFZ. Projection is oblique Mercator such that horizontal lines are parallel to predicted Pacific–Juan de Fuca plate motion.

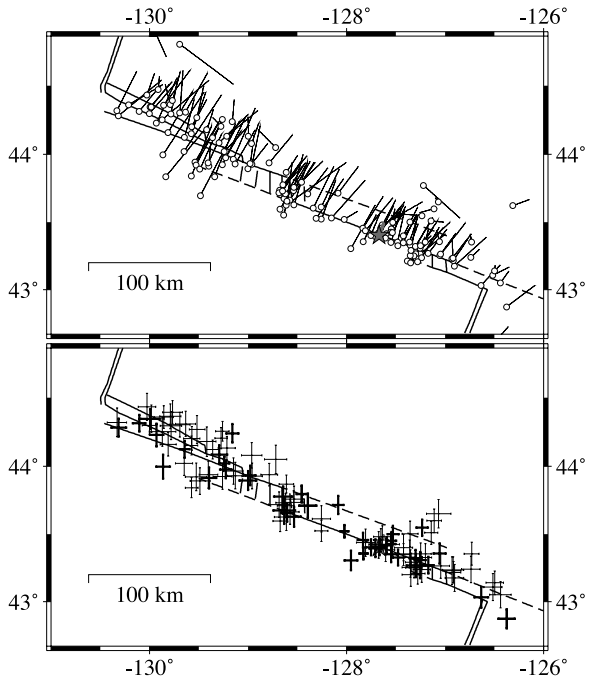

Figure 7. Epicenter relocations. (top) Open circles are relocated epicenters; thin lines point to original locations. Star shows the reference event location on Blanco Ridge with the thick gray line pointing to its ISC location. (bottom) Uncertainty bars of 123 well-relocated earthquakes (latitude and longitude uncertainties $\leq$ 12 km at 95% confidence level). Thick bars mark M $\geq$ 5 earthquakes, which are generally well relocated.

[23] The most severe location difference, marked by a star in Figure 8, was found for the largest BTFZ event since 1964, the M_w = 6.5 27 October 1994 earthquake (Table 2). The events' SOSUS location is about 70 km northwest of its JED epicenter. Our JED location along the eastern part of the Blanco Ridge agrees with the relocation by *Cronin and Sverdrup* [2003]. The earthquake had a long-rupture duration of about 20–25 s, inferred from the source time function (Figure 9) derived from teleseismic body wave analyses and from a ~10 s CMT centroid time shift [*Dziewonski et al.*, 1995]. Teleseismic analysis of P and SH waves using the method of *Nábělek* [1984] supports a rupture propagating unilaterally toward northwest with the maximum seismic moment release occurring late in the rupture and, depending on the actual rupture velocity, possibly about 40–60 km northwest of the epicenter. The region of maximum moment release, thus, occurred near the SOSUS location suggesting that the maximum T phase was generated in the vicinity of maximum moment release. SOSUS locations thus may not represent the correct epicenter for spatially extended sources.

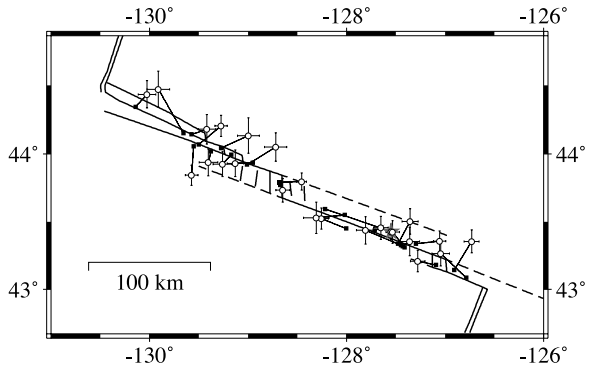

Figure 8. Comparison between JED and SOSUS locations for 24 common earthquakes. Open circles are relocated epicenters with thin lines connecting to their SOSUS locations (solid squares). Most SOSUS locations are outside the 95% confidence limits (solid bars) of JED relocations. The shaded star marks the relocation of the 27 October 1994 event about 70 km southeast of its SOSUS location.

[24] Our relocation of larger events (mainly $M_w \geq 5$) suggests that SOSUS earthquake location uncertainties could be larger than previously assumed [*Fox et al.*, 1995; *Johnson et al.*, 2000] and may involve systematic biases. Short T phases from small events appear more likely to result in accurate SOSUS locations as shown by successful response efforts after T phase detected earthquake swarms [*Dziak et al.*, 2006]. The resolution limit of teleseismic data and the small event set for which both locations exist currently precludes a more comprehensive evaluation of SOSUS location uncertainties.

3.2. Source Mechanism Overview, Slip Vector, and T Axes Orientations

[25] Separating strike-slip from normal faulting source mechanisms (Figure 10) reveals the systematic variation of deformation style along the BTFZ that mimics bathymetry and reflects changes between transform segments and intervening extensional basins. Most earthquakes have strike-slip mechanisms and occurred on transform segments (Figure 10, top). The eastern Blanco Ridge (127°–127.8°W) is the most active transform segment; the three largest events (M_w 6.4–6.5) also occurred there. In comparison, few strike-slip events ruptured along Blanco Ridge west of 127.8°W. Strike-slip mechanisms also occurred east of 127°W between the Gorda Ridge and the Gorda Depression and north of the eastern Blanco Ridge. Strike-slip events dominate west of ~129.2°W to the BTFZ-Juan de Fuca ridge intersection. Few strike-slip mechanisms were found near 128.75°W between the Cascadia and Surveyor depressions, an area otherwise dominated by normal fault-

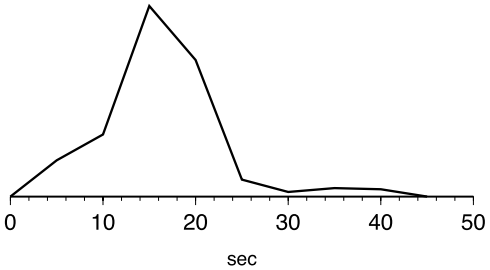

Figure 9. Apparent source time function (ASTF) for the 27 October 1994 M_w = 6.5 earthquake from teleseismic body wave analysis [*Nábělek*, 1984]. Best point source parameters are listed in Table 2; a northwest propagating rupture improves the fit to the data significantly, and the ASTF is for this model.

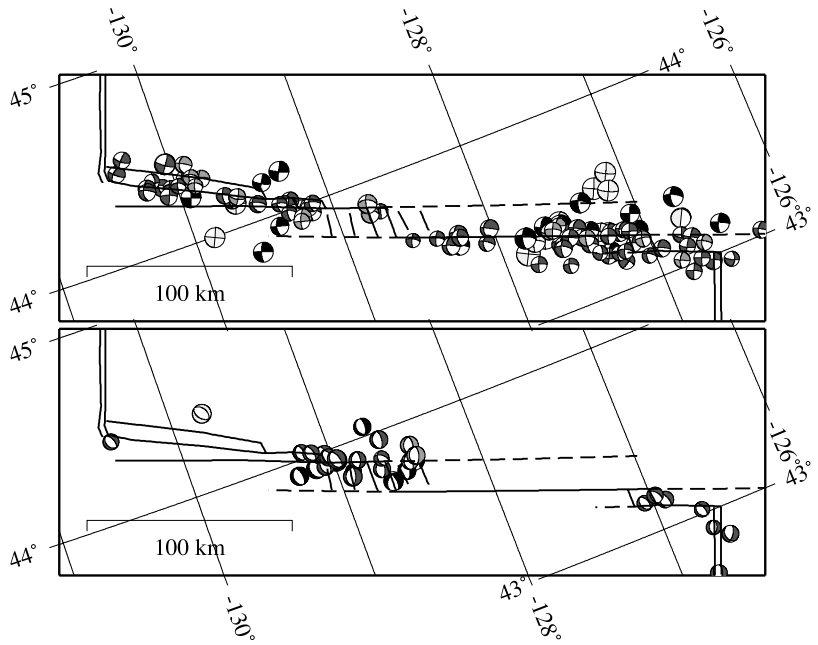

Figure 10. Fault plane solution map (lower hemisphere projection, size proportional to M_w). (top) Plot of 115 strike-slip, (bottom) plot of 31 normal faulting events. Black indicates relocated RMT solutions (latitude and longitude uncertainty $\leq$ 12 km); dark gray indicates RMTs on SOSUS location; medium gray indicates RMTs located with regional P and S arrival time data for events without SOSUS location; light gray indicates relocated CMT solutions. Events are listed in Tables 2 and 3.

ing earthquakes (Figure 10, bottom). Normal faulting events were also found along the Gorda Ridge, inside the Gorda Depression (near 127°W), and at the south tip of Juan de Fuca Ridge. The normal faulting mechanism of event 11 January 1989 (Table 3) east of 130°W is dubious. Its CMT solution has one of the highest moment tensor uncertainties and non double-couple contributions of all events in the CMT catalog; it is also the smallest CMT event along the BTFZ (M_w = 5.1) up to the end of 2005.

[26] The slip vector azimuths of the strike-slip events are highly consistent along the length of the BTFZ (Figure 11, top); their average orientation of 291° agrees with the predicted Pacific–Juan de Fuca plate motion direction of 290° [*Wilson*, 1993]. We even see a systematic variation of

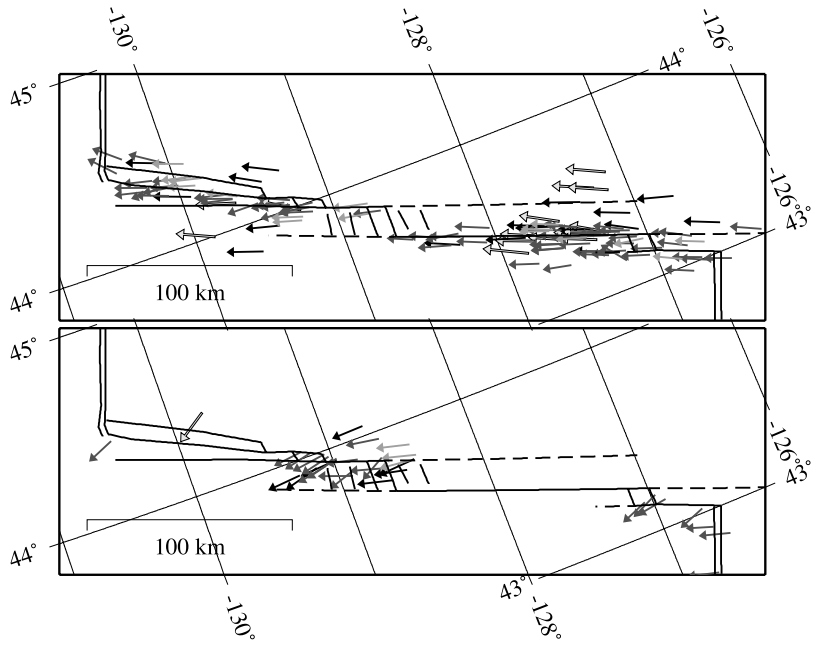

Figure 11. (top) Map of slip vector azimuths of the 115 strike slip earthquakes. (bottom) Map of T axis orientations of the 31 normal faulting events. Gray scheme is as in Figure 10.

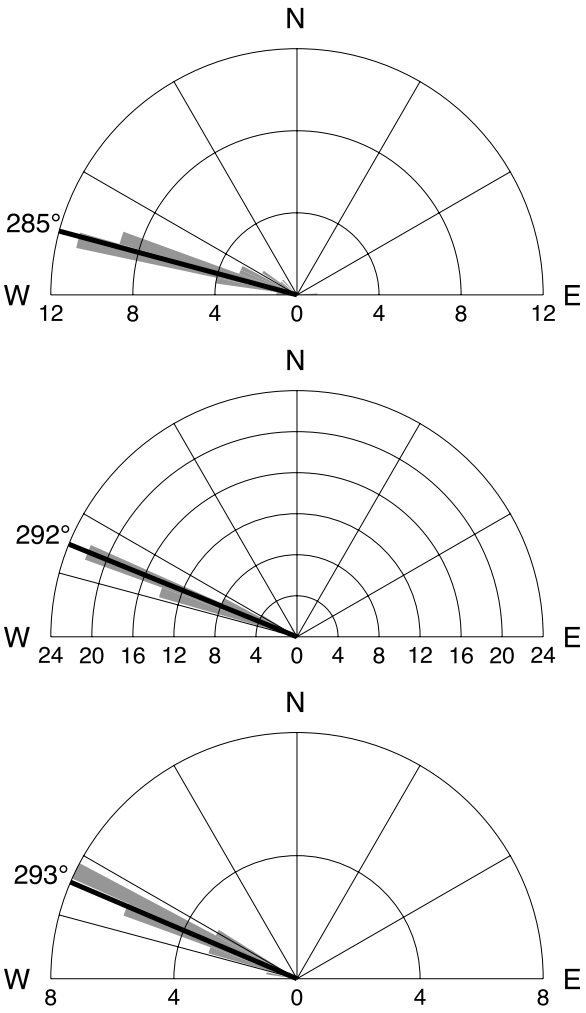

Figure 12. Rose diagram of slip vector azimuths for strike-slip earthquakes (top) west of 129°W, (middle) between 127.1°–128.6°W, and (bottom) east of 127°W. Observed azimuths (gray shaded area) are binned in 4° intervals; semicircles show number of events per bin. Note the narrow distribution in each group. The median azimuth (solid black line) rotates slightly clockwise from west to east (top to bottom) as predicted by plate motion models.

the median azimuth from 285° west of 129°W, to 292° along the Blanco Ridge, and to 293° east of 127.1°W (Figure 12), consistent with plate motion direction changes from 288° at the BTFZ-Juan de Fuca ridge to 292° at the BTFZ-Gorda ridge intersection [*Wilson*, 1993]. Resolving such small variations attests to the high overall quality of the RMT and CMT solutions. For RMTs, the strike of the northwest trending nodal plane and thus of the slip vector azimuth is well constrained by the seismic station distribution (i.e., the nodal plane runs through the network). Current Pacific–Juan de Fuca plate motion models are based solely on magnetic anomaly data [e.g., *Riddihough*, 1984; *Wilson*, 1993]. Our slip vector azimuths provide additional constraints for updates to these models.

[27] The RMT strike-slip solutions, although predominantly strike slip, show a consistent Juan de Fuca down motion (Figure 13, bottom; the average plunge is 19° with ±17° measurement standard deviation). Our plunges are significantly larger than for CMT solutions (Figure 13, bottom, average of 6°), which, however, also show a consistent Juan de Fuca down motion. For common events, the average RMT to CMT difference is 9° suggesting that our values could be systematically biased due to inadequacies of the velocity model. For cooling oceanic lithosphere differential plate subsidence is expected to occur such that the younger transform side subsides relative to the older side [e.g., *Fox and Gallo*, 1984] resulting in nonzero plunges during earthquake rupture for weak fault-normal coupling. In a symmetric ridge-transform-ridge setting, largest relative vertical motions along a transform should occur near the ridges and decrease toward its center. The lithosphere age relation along the young (<8 Ma), evolving BTFZ, however, is nonsymmetric [*Embley and Wilson*, 1992; *Wilson*, 1993]; the Juan de Fuca side is younger than the Pacific side along the western two thirds of the BTFZ, which could contribute to the observed dominance of the Juan de Fuca down motion. Along the Blanco Ridge (Figure 13, top), larger plunges seem concentrated near its intersection with the extensional Cascadia and Gorda depressions, suggesting that Juan de Fuca down motion near these tectonically controlled (discussed below) basins could exaggerate thermal subsidence effects.

[28] T axes orientations of normal faulting earthquakes fall into two groups (Figure 11, bottom). Events at the north tip of the Gorda Ridge and near the Cascadia Depression east of 129°W have T axes oriented at about 275°–290°, roughly parallel to the plate motion direction (290° [*Wilson*, 1993]), supporting the view that the Cascadia Depression is a small spreading center. On the other hand, events in the Gorda (near 127°W) and Surveyor depressions (west of 129°W) and the two events further west have 245°–270° T axes orientations oblique to the plate motion direction and to the orientation of transforms bordering these normal faulting regions. Their T axes orientation, though, agree with the oblique trend of bathymetric features inside the Gorda and Surveyor depressions [*Embley and Wilson*, 1992], indicating that they are pull-apart basins [*Mann et al.*, 1983; *Christie-Blick and Biddle*, 1985].

3.3. Centroid Depth Distribution

[29] Teleseismic body wave studies of OTF earthquakes show that the lower boundary of the seismic zone follows lithosphere age and thus depends on the thermal structure with a cutoff near the 600°C isotherm [e.g., *Wiens and Stein*, 1983; *Bergman and Solomon*, 1988; *Abercrombie and Ekström*, 2001, 2003]. The 600°C isotherm corresponds roughly to postulated transition from frictional behavior to ductile creep of olivine [*Pinkston and Kirby*, 1982; *Boettcher et al.*, 2007]. The RMT centroid depth distribution (Figure 2, bottom) constrains depth of the seismic zone along the BTFZ to 10 km or less with uncertainties of about ±3 km. For an average oceanic crustal thickness of ~6 km [*Chen*, 1992], the depth distribution implies events occurred in the crust and uppermost oceanic mantle.

[30] Our 5-year BTFZ monitoring allows detection of systematic seismic width variations along an entire OTF (Figure 14). Centroid depths near the ridge-transform intersections with the Gorda and the Juan de Fuca ridges are slightly shallower (4–6 km depth range) than in the central

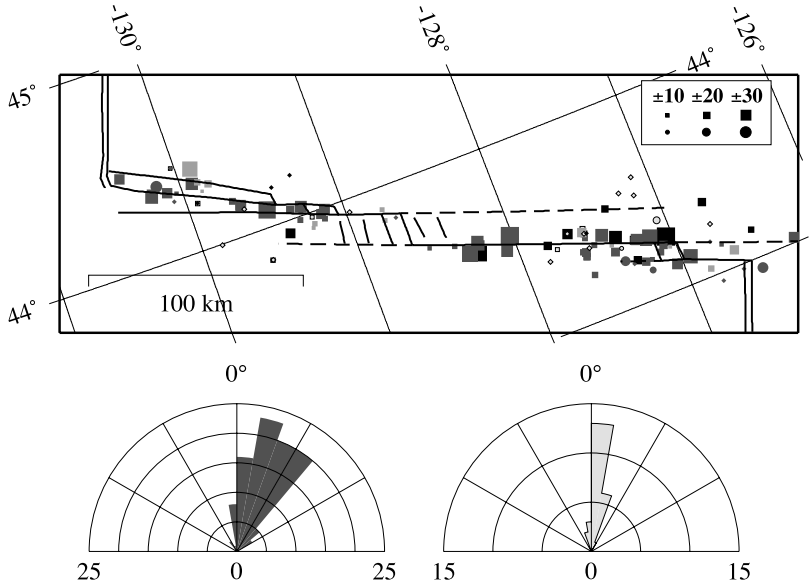

Figure 13. (top) Map of slip vector plunges for strike slip events (gray scheme is as in Figure 10). Squares denote Juan de Fuca plate down component relative to the Pacific plate during faulting, circles denote an up component; size proportional to plunge angle emphasizes large values. (bottom) (left) Plunge angles for RMT and (right) for CMT solutions. Events with Juan de Fuca plate down motion component plot right of center (0°); plunges in 10° bins. CMTs with $M_{xz} = M_{yz} = 0$ constraint (Table 3) are not included.

part of the BTFZ (4–9 km depth range). Shallowing of the lower boundary of the seismogenic zone is consistent with thermal models [e.g., *Chen*, 1988] predicting elevated isotherms near a ridge-transform intersection. We calculated the thermal structure along the BTFZ using a half-space cooling model [*McKenzie*, 1969; *Turcotte and Schubert*, 2002] averaging temperatures on either side of the transform to obtain isotherms shown in Figure 14 (middle). The isotherms assume spreading at the Juan de Fuca and the Gorda ridges and no thermal upwelling at the Cascadia Depression. Rupture areas, assuming a simple circular rupture model with constant slip-to-radius ratio (constant stress drop), are generally above the 600°C isotherm that appears to control the maximum depth of seismic slip consistent with other observations and experimental work on olivine frictional stability cited above. The average seismic zone width is 7.0 (8.7) km assuming seismic slip is confined between the 200°C (100°C) and 600°C isotherms. The 100°–200°C temperature range corresponds to the transition from aseismic stable sliding at shallow depth to deeper stick-slip behavior in serpentinite [*Moore et al.*, 2004; *Boettcher*, 2005]. The only significant deviation from the isotherm-based cutoff appears to occur for the $M_w = 6.5$, 27 October 1994 event (large ellipse in Figure 14, middle); for this large event, a circular rupture assumption is likely incorrect and the actual rupture probably had a large length-to-width ratio with significant slip along most of the western Blanco Ridge.

[31] The simple cooling model (Figure 14, middle) is consistent with the depth distribution showing a predominance of deeper events in the center of the BTFZ. The center area including the Surveyor and Cascadia depressions is dominated by normal faulting at well-resolved 6–9 km depth. Simple active spreading with a shallow magma chamber and thermal upwelling at the Cascadia Depression would raise the isotherms (Figure 14, bottom), which appears contradictory to the observed deep centroids. An explanation could be that the magma source is deep, with intermittent supply and rapid hydrothermal cooling following dike emplacement [*Coogan et al.*, 2005]. Seismicity to about 10 km depth is commonly observed at slow spreading centers. Microearthquakes at the northern Gorda Ridge reach 11 km depth [*Solano*, 1985], consistent with 9 km maximum depths obtained in our RMTs from the entire Gorda Ridge. OBS deployments at the slow spreading Mid-Atlantic Ridge near the Kane [*Toomey et al.*, 1985; 1988] and Oceanographer transforms [*Cessaro and Hussong*, 1986; *Barclay et al.*, 2001] show mainly 4–8 km focal depths and the depth range of coseismic faulting inferred from centroid depths of larger mid-ocean ridge earthquakes [*Huang et al.*, 1986; *Jemsek et al.*, 1986; *Huang and Solomon*, 1987, 1988] is about 2–10 km, all in the range we observe here.

3.4. Seismic Slip Rate Estimates

[32] Comparing observed cumulative seismic slip rates with the predicted BTFZ plate motion rate (56 mm/a [*Wilson*, 1993]) provides constraints on the amount of seismic slip versus aseismic creep and the thermomechanical properties of an OTF. On the basis of a global analysis of 65 OTFs, *Boettcher and Jordan* [2004] suggested that only about 15% of the overall plate motions are released seismically. A similar low percentage has been reported for the Eltanin fracture zone [*Stewart and Okal*, 1983; *Okal and Langenhorst*, 2000]. Other studies, however, found agreement between seismic and plate motion rates for the Gibbs fracture zone [*Kanamori and Stewart*, 1976], the Romanche and Jan Mayen transforms [*Brune*, 1968], the Romanche,

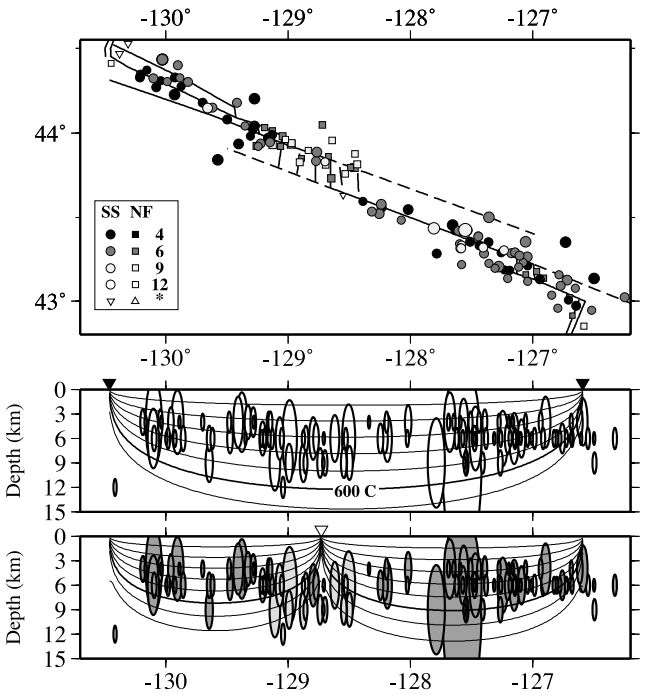

Figure 14. (top) Map of RMT centroid depth distribution along the BTFZ. SS are strike slip and NF normal faulting earthquakes; numbers are centroid depths in [km], Asterisk denotes centroid depth not resolved. (middle) Cross section of earthquake rupture areas projected onto the BTFZ; note shallowing toward the Juan de Fuca and Gorda ridges and the lack of 4 km shallow NF events. Inverted triangles mark BTFZ-Juan de Fuca and BTFZ-Gorda ridge intersections. Rupture areas were calculated for simple circular ruptures with constant slip-to-diameter ratio of 1.25×10^{-5} and rigidity of 3.5×10^{10} N/m^2; vertical exaggeration deforms circular ruptures to ellipsoids. Isotherms, calculated for a half-space cooling model and averaging across the transform, are shown as solid lines in 100°C increments; the bold line marks the 600°C isotherm; assumed diffusivity k = 10^{-12} km^2/s, half spreading rate of 28 mm/a, ridge offset of 350 km, and mantle temperature of 1300°C. (bottom) Same as Figure 14 (middle) but assuming that Cascadia Depression (inverted open triangle) is a spreading segment resetting isotherms to zero age; NF events (light gray) near Cascadia Depression are inconsistent with reset.

Bullard, and Conrad transforms [*Stewart and Okal*, 1981], and transforms in the Gulf of California [*Reichle et al.*, 1976; *Goff et al.*, 1987].

[33] Contradicting results exist for the BTFZ ranging from low to full coupling (see below). We, thus, reexamined the seismic slip rates by summing seismic moments of all 1774 earthquakes from 1964 to 2005 from the ISC, PDE, and Harvard catalogs and our RMT database; we extended the period (compared to our moment tensor analysis) to obtain representative long-term moment release estimates, although analysis of the 1964–1998 period provides almost identical results. The data seem complete only for $m_b \geq 4.4$–4.5. Constructing the laterally varying BTFZ slip rate distribution consists of four steps. We first projected all earthquakes within 50 km of the fault zone onto the BTFZ; nonrelocated events were corrected for average epicenter mislocation (Figures 6 and 7) before projection. Next, we converted all event magnitudes to seismic moment considering the observed magnitude bias (Figure 5) for events without direct M_w. We then distributed moments onto the BTFZ assuming constant rigidity μ = 35 GPa and rectangular fault geometry of fixed width W = 7 km. We distributed moment symmetrically around each epicenter projection point (mimicking bilateral rupture) assuming constant stress drop that relates slip u to rupture length L using a slip-to-length ratio of 1.25×10^{-5} from scaling relations [e.g., *Scholz*, 2002]. Finally, we summed contributions from all events in 1 km increments along the BTFZ. Over the large number of events the parameterization provides a smoothed version of the moment release distribution. The observed distribution is insensitive to changes in the slip-to-length ratio of a factor of 2 due to the distributed nature of the epicenters.

[34] The slip rate (Figure 15) along the BTFZ varies greatly. The variation mimics the epicenter distribution

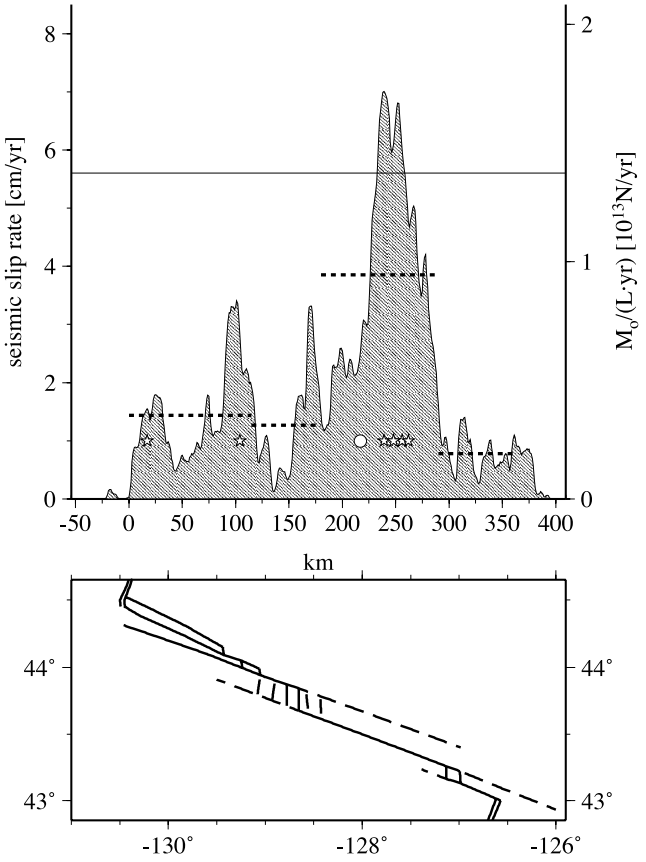

Figure 15. (top) Seismic slip rate distribution along the BTFZ for a uniformly 7 km thick seismic zone. The *x* axis is relative to 44.45°N, 130.4°W (approximately the BTFZ-Juan de Fuca ridge intersection). The horizontal line at slip rate 56 mm/a is the full plate motion rate [*Wilson*, 1993]. Stars show locations of 6 $M_w \geq 6$ events; circle denotes one m_b = 6.1 event (occurring 1968 predating CMT analysis). Earthquakes cover the 1964–2005 period. Dashed lines are averages for the four segments. (bottom) BTFZ overview map.

(Figure 7) and follows deformation style changes (Figure 10) further highlighting fault zone segmentation. The largest rates were observed along the Blanco Ridge transform segment where most large events (open stars $M_w > 6.0$, circle $m_b > 6.0$) occur that contribute significantly to the rate (km 180–290, Figure 15, the transform following Blanco Ridge is actually about 150 km long, we mapped earthquakes and their slip onto a single line and for this discussion divided it based on the dominant deformation style known from RMT and CMT solutions). The average Blanco Ridge rate of 3.9 cm/a accounts for most of the plate motion (solid horizontal line in Figure 15). Rates along Blanco Ridge differ east and west of ~128°W. To the east, the segment seems fully coupled (average 5.0 cm/a); to the west, fewer and generally smaller events occur and less than half of plate motions are accounted for seismically (average 2.2 cm/a).

[35] The observed slip rate along the West Blanco transform segment (km 0–115, Figure 15) is considerably lower (average 1.4 cm/a) than at the Blanco Ridge; different slip rates between the eastern and western BTFZ had also been noted by *Dziak et al.* [1991]. Considering different seismic zone widths (Figure 14, West Blanco ~6 km, Blanco Ridge ~9 km) reduces the discrepancy slightly resulting in average seismic slip rate estimates of 1.7 and 3.0 cm/a for the West Blanco and the Blanco Ridge segment, respectively. The discrepancy is possibly even smaller, because the earthquake frequency-size distribution differs for the two segments. The b value is larger for the West Blanco (b ~1.5) than for the Blanco Ridge (~1.0) segment [*Braunmiller*, 1998] such that small events, too small to be recorded by land stations, might contribute significantly to West Blanco seismic moment release. Extrapolating over all magnitudes [e.g., *Molnar*, 1979], including small nondetected events and assuming the frequency-magnitude relation holds, would result in similar rates along both segments that could account for the entire plate motions. Long-term OBS studies are necessary to detect and verify the occurrence rate of small events.

[36] Low rates accounting for only about 10–20% of plate motions were observed for segments with normal faulting events. From the Blanco Ridge to the BTFZ-Gorda ridge intersection (km 290–360, Figure 15), the average rate is 0.8 cm/a. The rate for the segment including the Cascadia and the Surveyor depressions (km 115–180, Figure 15) is 1.3 cm/a for lateral motion, which reduces to 0.9 cm/a assuming 45° dipping planes. Several stronger normal faulting earthquakes were located at the eastern boundary of the Cascadia Depression resulting in slightly higher rates between km 155 and 180 (Figure 15). It appears likely that most plate motions along extensional segments are accommodated by aseismic creep.

[37] OTFs are ideal areas to study temporal variations of spatial seismic slip distributions because of their high seismic activity and well-defined narrow deformation zones. We divided our 42-year data set in two 21-year segments (1964–1984, 1985–2005) recovering very similar slip distributions for both intervals and as in Figure 15. It seems the mapped distribution (Figure 15) reflects long-term seismic moment release patterns indicating long-lived coupling differences and thus differences in plate motion accommodation mechanisms.

[38] The average slip rate over the entire BTFZ is 2.0 cm/a (36% of the plate motion); a rate actually not observed for any segment illustrating that averaging over an entire transform fault system is a gross oversimplification. Three other studies estimated average slip rates along the BTFZ [*Hyndman and Weichert*, 1983; *Boettcher and Jordan*, 2004; *Willoughby and Hyndman*, 2005]. Each used different parameterizations to describe seismicity and seismic zone width. It is thus important to consider parameterization when comparing rates. *Boettcher and Jordan* [2004] suggested only about 10% of the BTFZ motion is seismic. The difference with our estimate is largely due to a wider seismic zone (10 km assumed by *Boettcher and Jordan* [2004] compared to 7 km determined in this study) and a higher rigidity (μ = 44.1 GPa appropriate for upper mantle compared to μ = 35 GPa, the average rigidity for the top 9 km of our model in Table 1 that includes oceanic crust). *Hyndman and Weichert* [1983] and *Willoughby and Hyndman* [2005] suggested seismicity could account for the entire plate motion if seismic width is 3–4 km narrow. On the basis of our depth distribution (Figure 14), average seismic width is larger by a factor of 2.

3.5. Fault Zone Segmentation

[39] We divide the BTFZ into four segments based on epicenter distribution (Figure 7) and variations of deformation style (Figure 10), centroid depth (Figure 14), and seismic slip rate (Figure 15). The segments, which we call the Gorda Depression, Blanco Ridge, Cascadia and Surveyor, and West Blanco segments, are not individual faults, but rather represent areas of similar deformation. Our proposed division, based on seismic data, agrees with bathymetry (Figure 16) and thus with the BTFZ segmentation proposed by *Embley and Wilson* [1992].

3.5.1. Gorda Depression Segment

[40] The easternmost segment (Figure 16) consists of a bathymetric basin immediately north and west of the Gorda Ridge-BTFZ intersection (near 43.0°N, 126.6°W) that is bounded by faults along its north and south walls. The basin deepens toward the Gorda Depression proper, centered near 127.1°W, and ends near 127.2°W. *Embley and Wilson* [1992] suggested the basin is a remnant spreading segment that was almost entirely replaced by the northward propagating Gorda Ridge to the east about 1–2 Ma ago. Observed earthquakes are generally shallow (4–6 km centroid), small ($M_w \leq 5.3$, 4.6 for strike-slip and normal faulting events, respectively, based on RMT and CMT analysis) and account for only about 15% of the plate motions. Normal faulting events were observed at the northern Gorda Ridge and in the Gorda Depression. None was large enough for relocation and we suspect all relocated events (including older events without mechanism) are strike slip. For the ~10 km narrow basin, relocation resolution does not uniquely constrain which basin-bounding scarp is an active transform. On the basis of morphology, *Embley and Wilson* [1992] suggested only the southern scarp is active implying a right step of the plate boundary at the Gorda Depression. The segment-perpendicular spread of strike-slip events and the segment's overall deep bathymetry, however, suggest both scarps might be active. Activity along both scarps is also supported by seismicity that continues past the basin. The basin's north wall is a southeastward continuation of the Blanco Ridge; a

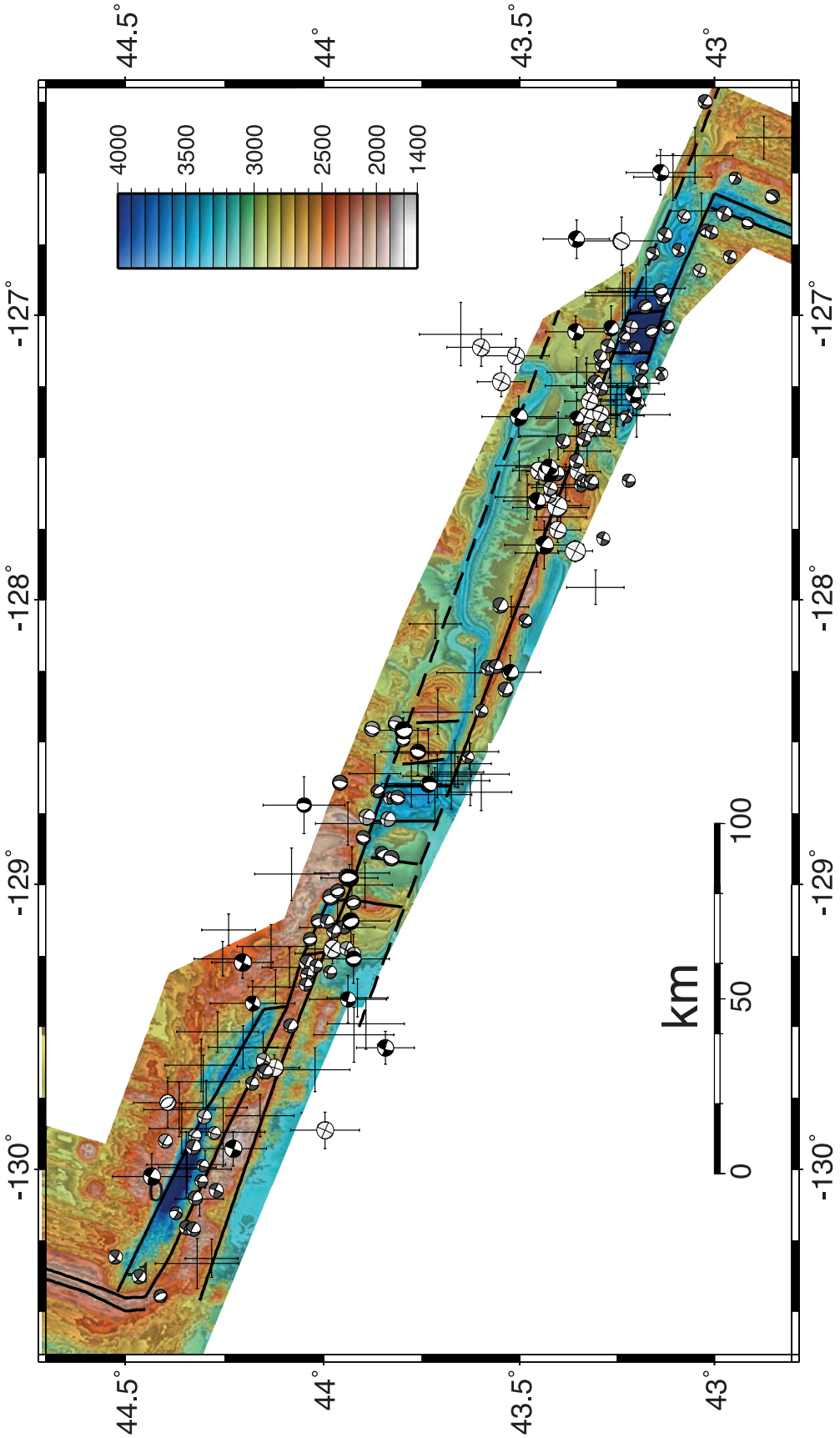

Figure 16. Close-up of the BTFZ. Plotted are fault plane solutions (gray scheme as in Figure 10) and well-relocated earthquake epicenters. SeaBeam data are from the RIDGE Multibeam Synthesis Project (http://imager.ldeo.columbia.edu) at the Lamont-Doherty Earth Observatory. Solid and dashed lines mark inferred [*Embley and Wilson*, 1992] locations of active and inactive faults, respectively.

single SOSUS-located strike-slip event near 43°N and 126.3°W implies the fracture zone east of the BTFZ-Gorda Ridge intersection is not aseismic. Several strike-slip events near 43.2°N and 127.2°–127.4°W south of the Blanco Ridge possibly occurred along a fault visible as bathymetric trough that extends from the southwest corner of the Gorda Depression toward west. Motion along the set of transforms is taken up as distributed extensional deformation inside the entire basin. The basin, based on its overall rhomb-shaped geometry, appears to be a mature pull-apart [*Mann et al.*, 1983]. The largest intrabasin events in the Gorda Depression are about $M_w \approx 4.5$ and most basin deformation is probably aseismic. The T axes are oriented about 245°–260° obliquely to the plate motion direction.

3.5.2. Blanco Ridge Segment

[41] The Blanco Ridge Segment consists of a transform fault that runs along the narrow ridge from Gorda Depression's north wall near 127.0°W to the southeast corner of the Cascadia Depression near 128.6°W (Figure 16). The Blanco Ridge Segment has been part of the BTFZ for 5 Ma and is the most stable part of it [*Embley and Wilson*, 1992]. The relocated epicenters follow the Blanco Ridge closely and all fault plane solutions are strike slip (Figure 10) with motion parallel (Figure 11) to the plate motion direction (291° [*Wilson*, 1993]).

[42] The seismic behavior changes sharply near 127.9°W. The eastern part is seismically very active and 5 out of 7 $M \geq 6$ earthquakes along the BTFZ occurred here. It is also the only transform fault part with strike-slip event centroid depths reaching 9 km indicating a wider seismic zone. High seismicity combined with abundance of large events results in full seismic coupling (Figure 15). West of 127.9°W, seismicity is much lower, earthquakes are generally smaller, seismic width narrows, and seismicity accounts for less than half of the plate motions. The transition between the two parts coincides closely with the western edge of Gorda Ridge-parallel abyssal hill topography on the Pacific plate, which is uplifted and merges with the Blanco Ridge near 127.5°–127.8°W [*Embley and Wilson*, 1992]. All large Blanco Ridge earthquakes nucleated in this structurally complex zone supporting the model of *King and Nábělek* [1985] that large earthquakes preferentially nucleate near fault zone geometrical complexities.

[43] Locations for a significant number of aftershocks exist only for the 27 October 1994 $M_w = 6.5$ earthquake, which was relocated near 127.55°W. SOSUS aftershock locations form a 70 km long band from about 127.8°W to the west tip of the Blanco Ridge near 128.7°W [*Dziak et al.*, 2000]. Assuming correct relative locations implies the main shock ruptured unilaterally toward northwest along the western part of the Blanco Ridge segment. Northwest unilateral rupture is supported by teleseismic body wave analysis. It is thus possible that large events nucleating near the fault zone complexity at 127.5°–127.8°W, rupture preferentially toward the northwest into the segment's seismically otherwise more quiet western part. Slip rate along the Blanco Ridge segment becomes more evenly distributed if we arbitrarily assume that all $M \geq 6$ earthquakes ruptured unilaterally toward northwest.

[44] Blanco Ridge is a prominent, transform-parallel ridge forming the plate boundary from the Cascadia to the Gorda depressions. Bathymetrically, Blanco Ridge extends further southeast to 126°W [*Embley and Wilson*, 1992]. Several mechanisms, involving serpentinite intrusions, volcanism due to extension, and dip-slip faulting due to spreading direction changes that cause across-fault extension or compression, were presented to explain the origin of such ridges [*Thompson and Melson*, 1972; *Bonatti*, 1976; 1978; *Bonatti et al.*, 1994; *Pockalny et al.*, 1996]. On the basis of single channel seismic reflection data, *Ibach* [1981] suggested Blanco Ridge is due to transform-normal compression. Our strike-slip fault plane solutions have a small normal-faulting component and thus are incompatible with across-fault compression. *Embley and Wilson* [1992] and *Dziak et al.* [2000] proposed the ridge is due to serpentinite diapirism caused by extensive shearing and subsequent water penetration into deeper parts of the crust. Petrologic samples from the central Blanco Ridge (near 127.5°–128°W) include lower crustal derived gabbros, indicating uplift, but no serpentinite possibly reflecting a sampling problem [*Dziak et al.*, 2000].

[45] Four relatively large ($M_w = 5.5–5.9$) strike-slip events were relocated near 43.5°N and 127.25°W (Figure 16) north of the Blanco Ridge. They align with a linear bathymetric feature that also forms the north wall of the Cascadia Depression and continues northwest where the lineament forms the south boundary of Parks Plateau (Figure 16). We relocated two additional earthquakes, one strike-slip near 126.75°W and one near 128.1°W, along this presumably inactive fracture zone. Our relocations imply the fracture zone is active east of the Cascadia Depression, which is consistent with a laterally offset turbidite channel (near 43.4°N and 127.25°W). Clustering of events near 127.25°W possibly reflects fault complexity. The lack of additional events is probably due to very small slip rates and long recurrence intervals.

3.5.3. Cascadia and Surveyor Segment

[46] Normal faulting earthquakes (Figure 16) dominate the segment between about 128.5°–129.2°W that includes the Cascadia and Surveyor depressions. We found only three strike-slip events at the north wall of the Cascadia Depression. Observed earthquakes are generally small ($M_w \leq 5.6$), relatively deep (6–9 km centroids) and account for less than 15% of plate motions. Normal faulting T axis orientations (Figure 11) change near 129°W from 275°–290° in the Cascadia Depression to about 245°–270° in the Surveyor Depression (Figures 11 and 16). T axis orientations in the Surveyor Depression are consistent with structural lineaments within the basin and indicate pull-apart deformation.

[47] The Cascadia Depression, the largest basin located in the central part of the BTFZ, might be a short spreading center and is interpreted to be a remnant of a south propagating ridge segment that dates back at least 5 Ma [*Embley and Wilson*, 1992]. Spreading is supported by basement doming and igneous intrusions within the basin's sediment fill that were inferred from seismic reflection data [*DeCharon*, 1989; *Embley and Wilson*, 1992]. The basins' inner valley floor is subsiding 1.8 cm/a for the last 6600 years [*Griggs and Kulm*, 1973], it is extending at a rate comparable to the Pacific–Juan de Fuca motion rate for the past 12,000 years [*DeCharon*, 1989], and it is seismically active (Figure 16) [also *Johnson and Jones*, 1978]. The depression's morphology with a central basin bordered

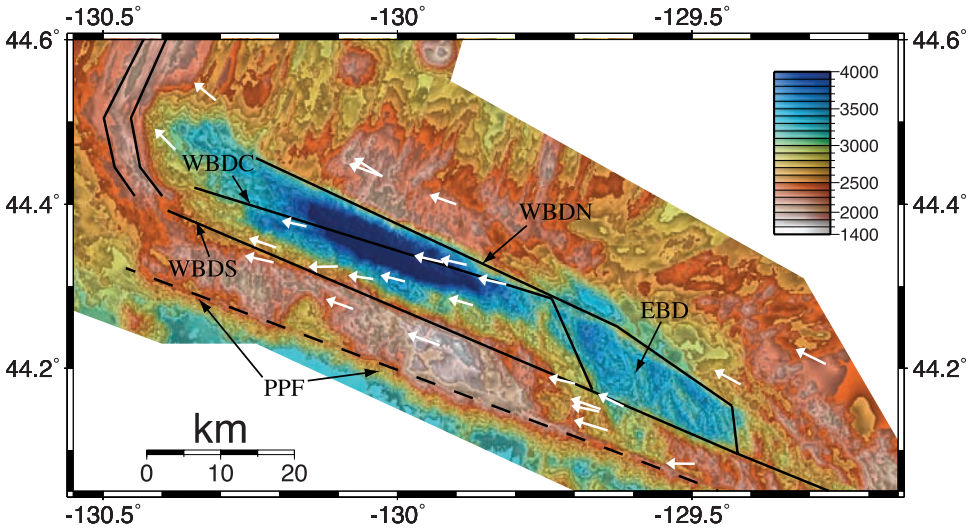

Figure 17. Close-up of the BTFZ-Juan de Fuca ridge-transform intersection. The deep basins are East Blanco Depression (EBD) and West Blanco Depression (WBD); the bathymetric high south of WBD is the Parks Plateau. White arrows are slip vector azimuths of strike-slip events (Figure 16) with tails at their epicenters. Possible active fault strands are shown schematically as solid and dashed lines and are marked (WBDN, WBDC, WBDS, and PPF); solid northerly trending lines illustrate right stepping of (some) transform motion at the EBD.

by inward facing back-tilted normal fault blocks [*Embley and Wilson*, 1992] is consistent with spreading. *DeCharon* [1989] proposed the lack of extrusives and the high subsidence rate could be explained by an episode of tectonic extension. Interpretation of the Cascadia Depression as a small spreading ridge is supported by earthquake T axes (275°–290°, Figure 11), which are almost parallel to the plate motion direction like along the Gorda Ridge spreading center and unlike the oblique trends observed within the Gorda and Surveyor pull-apart basins. Deep seismicity under the Cascadia Depression (Figure 14) and presence of stronger, normal faulting events at the depression's eastern boundary (Figure 16) indicate cool crust and hence the source of sporadic magmatism in the depression is probably deeper than the earthquakes. The last episodic intrusion probably occurred before about 6600 years ago and since then the center of the depression has been steadily subsiding. If water circulation cools the intrusion rapidly [*Coogan et al.*, 2005], the thermal imprint from intrusions can be minimal and may not affect maximum earthquake depth. This may explain why the simple cooling model fits the earthquake depth distribution better than the one including thermal upwelling at the Cascadia Depression (Figure 14). Overall, the characteristics of spreading in the Cascadia Depression resemble a slow spreading mid-ocean ridge (e.g., discussion by *Searle and Escartin* [2004]). The mechanical coupling of the western tip of the Blanco Ridge with the subsiding Cascadia Depression may cause the consistent down motion of the north side the transform revealed in the moment tensor strike-slip mechanisms from this area (Figure 13).

3.5.4. West Blanco Segment

[48] The region west of 129.2°W to the BTFZ-Juan de Fuca Ridge intersection is the West Blanco Segment (Figure 16). The segment includes two basins and several northwest trending linear features that might represent active transform fault traces. The basins are the pull-apart East Blanco Depression centered near 129.6°W and the West Blanco Depression (WBD) at the inner corner of the ridge-transform intersection. Observed earthquakes are shallow (4–6 km centroids), have strike-slip mechanisms, and account for one third of the plate motions.

[49] The West Blanco Segment is structurally more complex than the other segments. This was noted before and led to different models of the plate boundary configuration west of the Surveyor Depression. *Embley and Wilson* [1992] suggest significant reorganization in the geometry of the Western Blanco Segment in the last 0.4 Ma. At 1 Ma the main transform motion took place along the Parks Plateau Fault, a prominent escarpment at the southern edge of the Parks Plateau. They suggest a northward retreat of the Juan de Fuca Ridge caused transform faulting to shift northward into the West and East Blanco Depressions. Their present-day model has the main transform motion from Surveyor Depression stepping right at the East Blanco Depression and continuing along the 292°–295° trending north wall of the WBD (WBDN, Figure 17) to the Juan de Fuca Ridge. Other possible transform fault locations are the 292°–295° trending south wall of the WBD (WBDS, Figure 17) [*Embley and Wilson*, 1992; *Dziak et al.*, 2003], a 287°–288° trending lineation that runs obliquely through the WBD (WBDC, Figure 17) [*Dauteuil*, 1995], and the 290° trending lineation at the Parks Plateau Fault (PPF, Figure 17) [*Delaney et al.*, 1981]. The relocated epicenters are spread too widely to be consistent with seismicity along a single fault, but we cannot assign earthquakes to individual faults with confidence because teleseismic location uncertainties are large (±5–10 km) compared to the spacing of the proposed active faults (<10 km). Combining relocations and slip vectors, however, outlines three distinct groups with internally consistent relative motion that possibly define three active transform strands (Figure 17). The northern strand (WBDN)

runs along WBD's north wall; slip vector azimuths (290°–300°) generally agree with the trend of the wall. Submersible dives on the walls' central part revealed several outcrops with striated fault planes interpreted to represent active transform faulting [*Juteau et al.*, 1995]. The second strand (WBDC) is defined by a band of epicenters that runs from the northeast corner of the WBD obliquely through the depression to the Juan de Fuca ridge tip near 44.4°N and 130.4°W. The slip vector azimuths (median 283°) agree with the trend of the fault, which is a prominent feature in processed SeaBeam bathymetry [*Dauteuil*, 1995]. The southern strand (WBDS) follows the south wall of the WBD and terminates near the Juan de Fuca ridge tip. Although Parks Plateau lineament is covered by sedimented volcanic flows [*Juteau et al.*, 1995] and appears older, some relocated events (Figure 7) suggest Parks Plateau Fault may continue to be also active. It thus appears that reorganization of the Western Blanco Segment is ongoing and all four suggested transform fault strands could be active; the southern wall of the WBD seems seismically most active. SOSUS aftershock locations indicate that the 2 June 2000 M_w = 6.2 earthquake occurred along this strand [*Bohnenstiehl et al.*, 2002; *Dziak et al.*, 2003].

[50] The WBD differs morphologically from other BTFZ basins [*Embley and Wilson*, 1992] and is neither a pull-apart nor a spreading ridge. It is puzzling how the tremendous topographic relief could have been formed in the last 0.4 Ma particularly since no normal-faulting earthquakes have been identified here.

[51] Immediately at the WBD-Juan de Fuca Ridge intersection (west of 130.25°W, Figures 16 and 17), source mechanisms are slightly rotated. More northerly slip vectors (310° and 316°) suggest short transform segments are rotated toward the ridge axis. Similarly, the northwest-to-southeast oriented nodal planes of the normal faulting event at the Juan de Fuca Ridge' south tip suggests bending of the ridge toward the transform. Such geometrical adjustment directly at a ridge-transform intersection is reflected in the orientation of the seafloor bathymetry (Figure 17) and has been observed elsewhere [*Sonder and Pockalny*, 1999].

4. Summary and Conclusions

[52] The new seismological data presented for the Blanco Transform Fault Zone, consisting of reliable, waveform modeling derived moment tensor solutions, JED earthquake relocations, and along-fault zone earthquake slip rate estimates, represent the most comprehensive and detailed seismotectonic study of an entire oceanic transform fault system. The backbone of our study is regional moment tensor analysis, which lowered the threshold for determining earthquake source parameters by about one magnitude compared to teleseismic methods and resulted in a dense coverage of source parameters along the BTFZ. Relocation moved the earthquake epicenters closer to morphological structures and the faulting style, inferred from regional and teleseismic source parameters, is in excellent agreement with the morphology.

[53] The slip vector azimuths of the strike-slip earthquakes are very well resolved; they show small, systematic changes along the BTFZ that provide constraints for current Pacific–Juan de Fuca relative plate motion directions. The slip vector plunges show a consistent downward motion component of the Juan de Fuca relative to the Pacific plate along the entire BTFZ; although resolving slip vector plunges may be at the limit of the technique due to the simplified structure used to model regional waveforms. The observed predominance of Juan de Fuca down motion may be caused by the nonsymmetric age of the lithosphere, with Juan de Fuca side being younger along most of the length of the BTFZ. T axis orientations of normal faulting earthquakes define two spatially distinct groups. Events with T axes parallel to the relative plate motion direction occur along spreading centers and are observed along the Gorda Ridge and the Cascadia Depression; this observation is one of the main reasons why we concur with earlier work that Cascadia Depression is a short spreading segment. T axes of events inside the Gorda and the Surveyor Depressions are rotated by 45° and these depressions are interpreted as pull-apart basins.

[54] The earthquake depth distribution with 4–9 km deep centroids implies brittle deformation in the crust and uppermost oceanic mantle. Centroid depth variation along the BTFZ is consistent with a simple conductive cooling model with a cutoff depth for seismic slip near the 600°C isotherm. Deep (6–9 km) normal faulting events in the central part of the BTFZ under the Cascadia Depression would be difficult to explain if the depression were an active spreading center with shallow magma supply. We speculate that the magma source involved in spreading is deeper than the earthquakes. Dikes are injected only intermittently and rapidly cooled by water circulation and hence the thermal impact of magmatism is small. The region has been subsiding in the last 6600 years [*Griggs and Kulm*, 1973], indicating that the last magmatic episode occurred at least that long ago. In many ways, the Cascadia Depression resembles a slow spreading ridge.

[55] Slip rate mapping shows that seismic slip, and thus seismic coupling, is highly variable along the BTFZ. We suspect similar variability likely exists for other OTF systems, although this has not yet been documented. Seismic slip in extensional areas, the Gorda, Surveyor, Cascadia, and East Blanco depressions, accounts for only up to about 15% of plate motions; most deformation probably occurs as aseismic creep. Large earthquakes ($M_w \approx 5.6$) in extensional areas are significantly smaller than along stronger-coupled transform segments. The Blanco Ridge segment appears to be a relatively simple, single ~150 km long transform fault with a wider seismic zone compared to other segments; seismicity is high and larger earthquakes (up to M_w 6.4–6.5) occur frequently such that the segment, overall, seems nearly fully coupled. Transform motion along the western BTFZ is probably distributed along several, possibly shorter and narrow width transform faults limiting earthquake size to $M_w \leq 6.2$. Observed seismicity ($m_b \geq 4.5$) accounts for about 25% of plate motions requiring considerable aseismic creep, though, higher seismic coupling is possible if many small nondetected earthquakes as suggested by a large b value actually did occur.

[56] The different seismic behavior of the transform segments probably reflects their different history. The Blanco Ridge is a 5 Ma old, well-established transform fault. Seismicity, narrowly following a single fault, is high along the eastern part and drops significantly west of the area where shallow abyssal hill topography merges indicating

fault segmentation. Large earthquakes seem to nucleate preferentially near this fault zone complexity and possibly rupture mainly toward west into the seismically less active part of the Blanco Ridge.

[57] Seismicity of the Western Blanco Segment indicates that reorganization of this segment starting at about 0.4 Ma [*Embley and Wilson*, 1992] is still ongoing. We identify three active transform fault strands in the Western Blanco Depression along previously mapped faults. Moreover, there is indication for some continuing earthquake activity on the Parks Plateau Fault.

[58] Our detailed seismotectonic study of an entire OTF shows these systems can be complex with along-fault segmentation clearly manifested in variations of seismic properties that correlate with bathymetric changes. OTFs, in general, are thus probably not as simple as suggested by teleseismic analyses with their apparent simplicity merely reflecting lack of resolution. Additional and continued long-term studies near well-instrumented land settings (like the Juan de Fuca plate system) are necessary to gain a full understanding of OTFs.

[59] **Acknowledgments.** We thank A. Douglas for the JED program used in this study; J. Cassidy, R. Horner, and G. Rogers of the Geological Survey of Canada at the Pacific Geoscience center for broadband data from Vancouver Island; R. Dziak and C. Fox for SOSUS earthquake locations, A. Bobbitt and C. Fox (all at NOAA/PMEL) for help with an early version of bathymetric data; and B. Leitner for contributions in moment tensor determination and discussions at earlier stages of this work. Additional broadband waveform data were contributed by the Canadian Digital Seismic Network, Pacific Northwest Seismic Network, Berkeley Digital Seismic Network, and U. S. National Seismic Network. Plots were generated using the GMT plotting software [*Wessel and Smith*, 1995]. Constructive reviews by M. Boettcher, W. Wilcock, and D. Toomey are gratefully acknowledged. This research was supported by the NSF grant OCE-9521929.

References

Abercrombie, R., and G. Ekström (2001), Earthquake slip on oceanic transform faults, *Nature*, *410*, 74–77, doi:10.1038/35065064.

Abercrombie, R., and G. Ekström (2003), A reassessment of the rupture characteristics of oceanic transform earthquakes, *J. Geophys. Res.*, *108*(B5), 2225, doi:10.1029/2001JB000814.

Aki, K., and P. G. Richards (1980), *Quantitative Seismology: Theory and Methods*, vol. 1, W. H. Freeman, New York.

Barclay, A. H., D. R. Toomey, and S. C. Solomon (2001), Microearthquake characteristics and crustal VP/VS structure at the Mid-Atlantic Ridge, 35°N, *J. Geophys. Res.*, *106*, 2017–2034, doi:10.1029/2000JB900371.

Bergman, E. A., and S. C. Solomon (1988), Transform fault earthquakes in the north Atlantic: Source mechanisms and depth of faulting, *J. Geophys. Res.*, *93*, 9027–9057, doi:10.1029/JB093iB08p09027.

Bernardi, F., J. Braunmiller, U. Kradolfer, and D. Giardini (2004), Automatic regional moment tensor inversion in the European-Mediterranean region, *Geophys. J. Int.*, *157*, 703–716, doi:10.1111/j.1365-246X.2004.02215.x.

Beroza, G. C., and T. H. Jordan (1990), Searching for slow and silent earthquakes using free oscillations, *J. Geophys. Res.*, *95*, 2485–2510, doi:10.1029/JB095iB03p02485.

Biot, M. A. (1952), The interaction of Rayleigh and Stoneley waves in the ocean bottom, *Bull. Seismol. Soc. Am.*, *42*, 81–93.

Bird, P., Y. Y. Kagan, and D. D. Jackson (2002), Plate tectonics and earthquake potential of spreading ridges and oceanic transform faults, in *Plate Boundary Zones*, *Geodyn. Ser*, vol. 30, edited by S. Stein and J. T. Freymueller, pp. 201–218, AGU, Washington, D. C.

Boettcher, M. S. (2005), Slip on ridge transform faults: Insights from earthquakes and laboratory experiments, Ph.D. thesis, Mass. Inst. of Technol. and Woods Hole Oceanogr. Inst., Cambridge.

Boettcher, M. S., and T. H. Jordan (2004), Earthquake scaling relations for mid-ocean ridge transform faults, *J. Geophys. Res.*, *109*, B12302, doi:10.1029/2004JB003110.

Boettcher, M. S., G. Hirth, and B. Evans (2007), Olivine friction at the base of oceanic seismogenic zones, *J. Geophys. Res.*, *112*, B01205, doi:10.1029/2006JB004301.

Bohnenstiehl, D. R., M. Tolstoy, R. P. Dziak, C. G. Fox, and D. K. Smith (2002), Aftershock sequences in the mid-ocean ridge environment: An analysis using hydroacoustic data, *Tectonophysics*, *354*, 49–70, doi:10.1016/S0040-1951(02)00289-5.

Bolt, B. A., C. Lomnitz, and T. V. McEvilly (1968), Seismological evidence on the tectonics of central and northern California and the Mendocino escarpment, *Bull. Seismol. Soc. Am.*, *58*, 1735–1767.

Bonatti, E. (1976), Serpentinite protrusions in the oceanic crust, *Earth Planet. Sci. Lett.*, *32*, 107–113, doi:10.1016/0012-821X(76)90048-0.

Bonatti, E. (1978), Vertical tectonism in oceanic fracture zones, *Earth Planet. Sci. Lett.*, *37*, 369–379, doi:10.1016/0012-821X(78)90052-3.

Bonatti, E., M. Ligi, L. Gasperini, A. Peyve, Y. Raznitsin, and Y. J. Chen (1994), Transform migration and vertical tectonics at the Romanche fracture zone, equatorial Atlantic, *J. Geophys. Res.*, *99*, 21,779–21,802, doi:10.1029/94JB01178.

Bouchon, M. (1982), The complete synthesis of seismic crustal phases at regional distances, *J. Geophys. Res.*, *87*, 1735–1741, doi:10.1029/JB087iB03p01735.

Braunmiller, J. (1998), Seismotectonics of the Explorer region and of the Blanco Transform Fault Zone, Ph.D. thesis, Oreg. State Univ., Corvallis.

Braunmiller, J., and J. L. Nábělek (2002), Seismotectonics of the Explorer region, *J. Geophys. Res.*, *107*(B10), 2208, doi:10.1029/2001JB000220.

Braunmiller, J., J. L. Nábělek, B. Leitner, and A. Qamar (1995), The 1993 Klamath Falls, Oregon, earthquake sequence: Source mechanisms from regional data, *Geophys. Res. Lett.*, *22*, 105–108, doi:10.1029/94GL02844.

Brune, J. N. (1968), Seismic moment, seismicity, and rate of slip along major fault zones, *J. Geophys. Res.*, *73*, 777–784, doi:10.1029/JB073i002p00777.

Burr, N. C., and S. C. Solomon (1978), The relationship of source parameters of oceanic transform earthquakes to plate velocity and transform length, *J. Geophys. Res.*, *83*, 1193–1205, doi:10.1029/JB083iB03p01193.

Cessaro, R. K., and D. M. Hussong (1986), Transform seismicity at the intersection of the Oceanographer Fracture Zone and the Mid-Atlantic Ridge, *J. Geophys. Res.*, *91*, 4839–4853, doi:10.1029/JB091iB05p04839.

Chandra, U. (1974), Seismicity, earthquake mechanisms, and tectonics along the western coast of North America, from 42°N to 61°N, *Bull. Seismol. Soc. Am.*, *64*, 1529–1549.

Chen, Y. (1988), Thermal model of oceanic transform faults, *J. Geophys. Res.*, *93*, 8839–8851, doi:10.1029/JB093iB08p08839.

Chen, Y. J. (1992), Oceanic crustal thickness versus spreading rate, *Geophys. Res. Lett.*, *19*, 753–756, doi:10.1029/92GL00161.

Christie-Blick, N., and K. T. Biddle (1985), Deformation and basin formation along strike-slip faults, in *Strike-Slip Deformation, Basin Formation and Sedimentation*, edited by K. T. Biddle and N. Christie-Blick, *Spec. Publ. Soc. Econ. Paleontol. Mineral.*, *37*, 1–34.

Coogan, L. A., S. A. Kasemann, and S. Chakraborty (2005), Rates of hydrothermal cooling of new oceanic upper crust derived from lithium-geospeedometry, *Earth Planet. Sci. Lett.*, *240*, 415–424, doi:10.1016/jepsl.2005.09.020.

Cronin, V. S., and K. A. Sverdrup (2003), Multiple-event relocation of historic earthquakes along the Blanco Transform Fault Zone, NE Pacific, *Geophys. Res. Lett.*, *30*(19), 2001, doi:10.1029/2003GL018086.

Dauteuil, O. (1995), Fault pattern from SeaBeam processing: The western part of the Blanco fracture zone (NE Pacific), *Mar. Geophys. Res.*, *17*, 17–35, doi:10.1007/BF01268049.

DeCharon, A. V. (1989), Structure and tectonics of Cascadia segment, central Blanco Transform Fault Zone, M.S. thesis, pp. 73, Oreg. State Univ., Corvallis.

Delaney, J. R., H. P. Johnson, and J. L. Karsten (1981), The Juan de Fuca ridge-hot spot-propagating rift system: New tectonic, geochemical, and magnetic data, *J. Geophys. Res.*, *86*, 11,747–11,750, doi:10.1029/JB086iB12p11747.

Dewey, J. W. (1972), Seismicity and tectonics of western Venezuela, *Bull. Seismol. Soc. Am.*, *62*, 1711–1752.

Douglas, A. (1967), Joint epicentre determination, *Nature*, *215*, 47–48, doi:10.1038/215047a0.

Dziak, R. P., C. G. Fox, and R. W. Embley (1991), Relationship between the seismicity and geologic structure of the Blanco Transform Fault Zone, *Mar. Geophys. Res.*, *13*, 203–208, doi:10.1007/BF00369149.

Dziak, R. P., C. G. Fox, R. W. Embley, J. E. Lupton, G. C. Johnson, W. W. Chadwick, and R. A. Koski (1996), Detection of and response to a probable volcanogenic T-wave event swarm on the western Blanco Transform Fault Zone, *Geophys. Res. Lett.*, *23*, 873–876, doi:10.1029/96GL00240.

Dziak, R. P., C. G. Fox, R. W. Embley, J. L. Nábělek, J. Braunmiller, and R. A. Koski (2000), Recent tectonics of the Blanco Ridge, eastern Blanco transform fault zone, *Mar. Geophys. Res.*, *21*, 423–450, doi:10.1023/A:1026545910893.

Dziak, R. P., W. W. Chadwick, C. G. Fox, and R. W. Embley (2003), Hydrothermal temperature changes at the southern Juan de Fuca Ridge associated with Mw 6.2 Blanco transform earthquake, *Geology*, *31*, 119–122, doi:10.1130/0091-7613(2003)031<0119:HTCATS>2.0.CO;2.

Dziak, R., J. Cowen, E. Baker, D. Bohnenstiehl, B. Chadwick, J. Resing, and R. Embley (2006), Detecting volcanic events in the northeast Pacific, *Eos Trans. AGU*, *87*, 37–42, doi:10.1029/2006EO040001.

Dziewonski, A. M., G. Ekström, and M. P. Salganik (1994), Centroid-moment tensor solutions for October–December, 1993, *Phys Earth Planet Inter*, *85*, 215–225, doi:10.1016/0031-9201(94)90114-7.

Dziewonski, A. M., G. Ekström, and M. P. Salganik (1995), Centroid-moment tensor solutions for October-December, 1994, *Phys Earth Planet Inter*, *91*, 187–201, doi:10.1016/0031-9201(95)03081-7.

Ekström, G., and A. M. Dziewonski (1988), Evidence of bias in estimation of earthquake size, *Nature*, *332*, 319–323, doi:10.1038/332319a0.

Embley, R. W., and D. S. Wilson (1992), Morphology of the Blanco Transform Fault Zone-NE Pacific: Implications for its tectonic evolution, *Mar. Geophys. Res.*, *14*, 25–45, doi:10.1007/BF01674064.

Embley, R. W., W. W. Chadwick, I. R. Jonasson, D. A. Butterfield, and E. T. Baker (1995), Initial results of the rapid response to the 1993 CoAxial event: Relationships between hydrothermal and volcanic processes, *Geophys. Res. Lett.*, *22*, 143–146, doi:10.1029/94GL02281.

Engeln, J. F., D. A. Wiens, and S. Stein (1986), Mechanisms and depths of Atlantic transform earthquakes, *J. Geophys. Res.*, *91*, 548–577, doi:10.1029/JB091iB01p00548.

Fox, C. G., R. P. Dziak, H. Matsumoto, and A. E. Schreiner (1994), Potential for monitoring low-level seismicity on the Juan de Fuca ridge using military hydrophone arrays, *Mar. Technol. Soc. J.*, *27*, 22–30.

Fox, C. G., W. E. Radford, R. P. Dziak, T.-K. Lau, H. Matsumoto, and A. E. Schreiner (1995), Acoustic detection of a seafloor spreading episode on the Juan de Fuca ridge using military hydrophone arrays, *Geophys. Res. Lett.*, *22*, 131–134, doi:10.1029/94GL02059.

Fox, P. J., and D. G. Gallo (1984), Tectonic model for ridge-transform-ridge plate boundaries: Implications for the structure of oceanic lithosphere, *Tectonophysics*, *104*, 205–243, doi:10.1016/0040-1951(84)90124-0.

Goff, J. A., E. A. Bergman, and S. C. Solomon (1987), Earthquake source mechanisms and transform fault tectonics in the Gulf of California, *J. Geophys. Res.*, *92*, 10,485–10,510, doi:10.1029/JB092iB10p10485.

Griggs, G. B., and L. D. Kulm (1973), Origin and development of Cascadia deep-sea channel, *J. Geophys. Res.*, *78*, 6325–6339, doi:10.1029/JC078i027p06325.

Hanks, T. C., and H. Kanamori (1979), Moment magnitude scale, *J. Geophys. Res.*, *84*, 2348–2350, doi:10.1029/JB084iB05p02348.

Helffrich, G. R. (1997), How good are routinely determined focal mechanisms? Empirical statistics based on a comparison of Harvard, USGS, and ERI moment tensors, *Geophys. J. Int.*, *131*, 741–750, doi:10.1111/j.1365-246X.1997.tb06609.x.

Huang, P. Y., and S. C. Solomon (1987), Centroid depths of mid-ocean ridge earthquakes in the Indian Ocean, Gulf of Aden, and Red Sea, *J. Geophys. Res.*, *92*, 1361–1382, doi:10.1029/JB092iB02p01361.

Huang, P. Y., and S. C. Solomon (1988), Centroid depths of mid-ocean ridge earthquakes: Dependence on spreading rate, *J. Geophys. Res.*, *93*, 13,445–13,447, doi:10.1029/JB093iB11p13445.

Huang, P. Y., S. C. Solomon, E. A. Bergman, and J. L. Nabelek (1986), Focal depths and mechanisms of Mid-Atlantic ridge earthquakes from body wave inversion, *J. Geophys. Res.*, *91*, 579–598, doi:10.1029/JB091iB01p00579.

Hyndman, R. D., and D. H. Weichert (1983), Seismicity and rates of relative motion on the plate boundaries of western North America, *Geophys. J. R. Astron. Soc.*, *73*, 59–82.

Ibach, D. H. (1981), The structure and tectonics of the Blanco Fracture Zone, M.S. thesis, 60 pp., Oreg. State Univ., Corvallis.

Jemsek, J. P., E. A. Bergman, J. L. Nabelek, and S. C. Solomon (1986), Focal depths and mechanisms of large earthquakes on the Arctic mid-ocean ridge system, *J. Geophys. Res.*, *91*, 13,993–14,005, doi:10.1029/JB091iB14p13993.

Johnson, H. P., P. Hutnak, R. P. Dziak, C. G. Fox, I. Urcuyo, J. P. Cowen, J. Nabelek, and C. Fisher (2000), Earthquake-induced changes in a hydrothermal system on the Juan de Fuca mid-ocean ridge, *Nature*, *407*, 174–177, doi:10.1038/35025040.

Johnson, R. H., R. A. Norris, and F. K. Duennebier (1967), Abysally generated T-phases, *Rep. HIG-67-1*, Hawaii Inst. Geophys., Honolulu.

Johnson, S. H., and P. R. Jones (1978), Microearthquakes located on the Blanco fracture zone with sonobuoy arrays, *J. Geophys. Res.*, *83*, 255–261, doi:10.1029/JB083iB01p00255.

Juteau, T., D. Bideau, O. Dauteuil, G. Manach, D. D. Naidoo, P. Nehlig, H. Ondreas, M. A. Tivey, K. X. Whipple, and J. R. Delaney (1995), A submersible study in the Western Blanco Fracture Zone, N. E. Pacific: Structure and evolution during the last 1.6 Ma, *Mar. Geophys. Res.*, *17*, 399–430, doi:10.1007/BF01371786.

Kanamori, H., and G. S. Stewart (1976), Mode of strain release along the Gibbs fracture zone, Mid-Atlantic ridge, *Phys Earth Planet Inter*, *11*, 312–332, doi:10.1016/0031-9201(76)90018-2.

King, G. C. P., and J. L. Nábělek (1985), The role of bends in faults in the initiation and termination of earthquake rupture, *Science*, *228*, 984–987, doi:10.1126/science.228.4702.984.

Langenhorst, A. R., and E. A. Okal (2002), Correlation of beta-value with spreading rate for strike-slip earthquakes of the mid-oceanic ridge system, in *Plate Boundary Zones*, *Geodyn. Ser*, vol. 30, edited by S. Stein and J. T. Freymueller, pp. 191–202, AGU, Washington, D. C.

Ligi, M., E. Bonatti, L. Gasperini, and A. N. Poliakov (2002), Oceanic broad multifault transform plate boundaries, *Geology*, *30*, 11–14, doi:10.1130/0091-7613(2002)030<0011:OBMTPB>2.0.CO;2.

Mann, P., M. R. Hempton, D. C. Bradley, and K. Burke (1983), Development of pull-apart basins, *J. Geol.*, *91*, 529–554.

McKenzie, D. P. (1969), Speculations on the consequences and causes of plate motions, *Geophys. J. R. Astron. Soc.*, *18*, 1–32.

Molnar, P. (1979), Earthquake recurrence intervals and plate tectonics, *Bull. Seismol. Soc. Am.*, *69*, 115–133.

Moore, D. E., D. A. Lockner, H. Tanaka, and K. Iwata (2004), The coefficient of friction of chrysotile gouge at seismogenic depths, *Int. Geol. Rev.*, *46*, 385–398, doi:10.2747/0020-6814.46.5.385.

Nábělek, J. L. (1984), Determination of earthquake source parameters from inversion of body waves, Ph.D. thesis, Mass. Inst. of Technol., Cambridge.

Nábělek, J., and G. Xia (1995), Moment-tensor analysis using regional data: Application to the 25 March, 1993, Scotts Mills, Oregon earthquake, *Geophys. Res. Lett.*, *22*, 13–16, doi:10.1029/94GL02760.

Okal, E. A., and A. R. Langenhorst (2000), Seismic properties of the Eltanin transform system, South Pacific, *Phys Earth Planet Inter*, *119*, 185–208, doi:10.1016/S0031-9201(99)00169-7.

Okal, E. A., and L. M. Stewart (1982), Slow earthquakes along oceanic fracture zones: Evidence for asthenospheric flow away from hot spots?, *Earth Planet. Sci. Lett.*, *57*, 75–87, doi:10.1016/0012-821X(82)90174-1.

Pinkston, J., and S. H. Kirby (1982), Experimental deformation of dunite under conditions appropriate to the lithosphere, *Eos Trans. AGU*, *63*, 1094.

Pockalny, R., R. Detrick, and P. Fox (1988), Morphology and tectonics of the Kane transform from SeaBeam bathymetry data, *J. Geophys. Res.*, *93*, 3179–3193, doi:10.1029/JB093iB04p03179.

Pockalny, R. A., P. Gente, and R. Buck (1996), Oceanic transverse ridges: A flexural response to fracture-zone-normal extension, *Geology*, *24*, 71–74, doi:10.1130/0091-7613(1996)024<0071:OTRAFR>2.3.CO;2.

Reichle, M. S., G. F. Sharman, and J. N. Brune (1976), Sonobuoy and teleseismic study of Gulf of California transform fault earthquake sequences, *Bull. Seismol. Soc. Am.*, *66*, 1623–1640.

Riddihough, R. P. (1984), Recent movements of the Juan de Fuca plate system, *J. Geophys. Res.*, *89*, 6980–6994, doi:10.1029/JB089iB08p06980.

Scholz, C. H. (2002), *The Mechanics of Earthquakes and Faulting*, 2nd ed., Cambridge Univ. Press, New York.

Searle, R. C., and J. Escartin (2004), The rheology and morphology of oceanic lithosphere and mid-ocean ridges, in *Mid-ocean ridges: Hydrothermal interactions between the lithosphere and the oceans*, *Geophys. Monograph*, vol. 148, edited by C. R. German, J. Lin, and L. M. Parson, pp. 63–93, AGU, Washington, D. C.

Solano, A. E. (1985), Crustal structure and seismicity of the Gorda Ridge, Ph.D. thesis, Oregon State Univ., Corvallis, Oregon.

Sonder, L. J., and R. A. Pockalny (1999), Anomalously rotated abyssal hills along active transforms: Distributed deformation of oceanic lithosphere, *Geology*, *27*, 1003–1006, doi:10.1130/0091-7613(1999)027<1003:ARAHAA>2.3.CO;2.

Soukup, D. J., and R. I. Odom (2001), Continuum spectrum and radiation pattern contributions to T-wave excitation, *Eos Trans. AGU*, *82*(47), Fall Meeting Suppl., Abstract S21A-0556.

Stewart, L. M., and E. A. Okal (1981), Do all transform faults exhibit m_b-M_s disparity?, *Eos Trans. AGU*, *62*, 1031–1032.

Stewart, L. M., and E. A. Okal (1983), Seismicity and aseismic slip along the Eltanin Fracture Zone, *J. Geophys. Res.*, *88*, 10,495–10,507, doi:10.1029/JB088iB12p10495.

Thompson, G., and W. G. Melson (1972), The petrology of oceanic crust across fracture zones in the Atlantic Ocean: Evidence for a new kind of seafloor spreading, *J. Geol.*, *80*, 526–538.

Tobin, D. G., and L. R. Sykes (1968), Seismicity and tectonics of the Northeast Pacific ocean, *J. Geophys. Res.*, *73*, 3821–3845, doi:10.1029/JB073i012p03821.

Tolstoy, I., and M. Ewing (1950), The T-Phase of shallow focus earthquakes, *Bull. Seismol. Soc. Am.*, *40*, 25–51.

Toomey, D. R., S. C. Solomon, G. M. Purdy, and M. H. Murray (1985), Microearthquakes beneath the Median Valley of the Mid-Atlantic Ridge

near 23°N: Hypocenters and focal mechanisms, *J. Geophys. Res.*, *90*, 5443–5458, doi:10.1029/JB090iB07p05443.

Toomey, D. R., S. C. Solomon, G. M. Purdy, and M. H. Murray (1988), Microearthquakes beneath the Median Valley of the Mid-Atlantic Ridge near 23°N: Tomography and Tectonics, *J. Geophys. Res.*, *93*, 9093–9112, doi:10.1029/JB093iB08p09093.

Tréhu, A. M., and S. C. Solomon (1983), Earthquakes in the Orozco transform zone: Seismicity, source mechanisms, and tectonics, *J. Geophys. Res.*, *88*, 8203–8225, doi:10.1029/JB088iB10p08203.

Turcotte, D. L., and G. Schubert (2002), *Geodynamics*, 2nd ed., Cambridge Univ. Press, New York.

Wessel, P., and W. H. F. Smith (1995), New version of the generic mapping tools released, *Eos Trans. AGU*, *76*, 329, doi:10.1029/95EO00198.

Wiens, D. A., and S. Stein (1983), Age dependence of oceanic intraplate seismicity and implications for lithospheric evolution, *J. Geophys. Res.*, *88*, 6455–6468, doi:10.1029/JB088iB08p06455.

Wilcock, W. S. D., G. M. Purdy, and S. C. Solomon (1990), Microearthquake evidence for extension across the Kane transform fault, *J. Geophys. Res.*, *95*, 15,439–15,462, doi:10.1029/JB095iB10p15439.

Willoughby, E. C., and R. D. Hyndman (2005), Earthquake rate, slip rate, and the effective seismic thickness for oceanic transform faults of the Juan de Fuca plate system, *Geophys. J. Int.*, *160*, 855–868, doi:10.1111/j.1365-246X.2005.02523.x.

Wilson, D. S. (1993), Confidence intervals for motion and deformation of the Juan de Fuca plate, *J. Geophys. Res.*, *98*, 16,053–16,071, doi:10.1029/93JB01227.

Wolfe, C. J., E. A. Bergman, and S. C. Solomon (1993), Oceanic transform earthquakes with unusual mechanisms and locations: Relation to fault geometry and state of stress in the adjacent lithosphere, *J. Geophys. Res.*, *98*, 16,187–16,211, doi:10.1029/93JB00887.

J. Braunmiller and J. Nábělek, College of Oceanic and Atmospheric Sciences, Oregon State University, Corvallis, OR 97331-5503, USA. (jbraunmiller@coas.oregonstate.edu)